Microstructural evolution in ODS-EUROFER steel caused by high-dose He ion implantations with systematic variation of implantation parameters

O.V. Emelyanova [a,b,c], A. Gentils [a,*], V.A. Borodin [b,d], P.S. Dzhumaev [b], P.V. Vladimirov [e], R. Lindau [e], A. Möslang [e]

[a] *Université Paris-Saclay, CNRS/IN2P3, IJCLab, 91405 Orsay, France*
[b] *National Research Nuclear University MEPhI, 115409 Moscow, Russia*
[c] *Shubnikov Institute of Crystallography of Federal Scientific Research Centre "Crystallography and Photonics" of Russian Academy of Sciences, 119333 Moscow, Russia*
[d] *National Research Centre 'Kurchatov institute', 123182 Moscow, Russia*
[e] *Karlsruhe Institute of Technology (KIT), Institute for Applied Materials – Applied Materials Physics (IAM-AWP), 76344 Eggenstein-Leopoldshafen, Germany*

ARTICLE INFO

ABSTRACT

The paper presents a detailed analysis of helium (He) bubble development in ODS-EUROFER steel caused by helium ion implantation in different regimes, with a particular attention to the role of the oxide nanoparticles in promoting the growth of He bubbles, helium accumulation and gas-driven swelling. The Transmission Electron Microscopy (TEM) characterization of steel samples implanted applying systematic variation of experimental parameters has allowed clarifying the trends of the bubble microstructure evolution depending on the implantation dose, flux, and sample temperature. It was found that in all investigated implantation regimes He bubbles formed both in the grain bulk and on various structural defects (dislocations, grain boundaries, oxide particles and carbide precipitates), but the sizes and densities of bubbles in different bubble populations were sensitive to particular irradiation conditions. In the majority of cases the main traps for implanted helium and the main contributors to the estimated swelling were bubbles associated with grain boundaries, though in some cases (high implantation dose or lower temperature) the bubbles in the grain bulk were competitive with the grain boundary bubble population. Oxide particles in ODS-EUROFER were found to be excellent nucleation sites for He bubbles and practically each observed particle hosted a single relatively large bubble, sometimes as large as the particle itself. However, the contribution of oxide-associated bubbles to the estimated swelling and He inventory was found to be minor as compared to other bubble populations because of a relatively low number density of nano-oxides. Comparison of ODS-EUROFER and EUROFER 97 samples implanted with He ions in identical regimes has demonstrated lower efficiency of ODS-EUROFER for accumulating implanted helium in bubbles and noticeably higher share of helium atoms trapped in the vacancy defects invisible by TEM.

Introduction

The challenges of meeting rapidly growing demand for energy have renewed a worldwide interest in advanced power energy plants, while the need for new clean sources of energy provides strong support to the quest for next generation energy devices. Given the advantages of a high efficiency and fewer limitations from environmental impact, advanced fusion and fission (Gen IV) facilities, as well as accelerator driven systems (ADS) have a great potential to become an important part of the current and future non-carbon energy sources with continuous mode of energy generation [1–3]. The expected operation conditions of advanced fission and fusion facilities are characterized by high temperatures (~550–1000 °C), intense neutron radiation (~5–30 dpa/fpy, i.e. displacements per atom per full power year) and utilization of chemically aggressive coolants. Structural materials used in the current nuclear reactors (such as zirconium or austenitic stainless steels) have serious drawbacks as possible candidates for these heavy-duty operation applications.

Among the primary candidate structural materials considered for the forthcoming fusion and fission facilities are the ferritic-martensitic steels [4–6]. However, some reactor designs are expected to operate at temperatures well above the limit (~550 °C) of reliable mechanical

performance of these steels. According to modern views, one of the keys to improve the properties of multifunctional steels is strengthening with a very high density of ultrafine oxide nanoparticles [7–12]. More detailed research has shown that the high density of nano-oxide particles dispersed in the steel matrix not only improves its mechanical properties for high-temperature applications, but also adds to radiation stability of oxide-dispersion strengthened (ODS) steel [8].

However, in spite of intense international research on ODS steels in the last two decades, some fundamental questions concerning the nano-oxides usage for the improvement of the steel properties remain under debate. In addition to strengthening, nano-oxides in the steel matrix can affect the other modes of steel response (swelling, creep, fracture toughness, etc.) to the action of complex irradiation environments where the intensive displacement damage is accompanied with the accumulation of extremely high levels of light gases - helium and hydrogen. For example, for DEMO fusion reactor blanket system, $\sim$10 appm He/dpa and 40 appm H/dpa are expected [13]. While hydrogen accumulation in steels is not generally considered as a serious issue, the accumulation of very high concentrations of helium bears potential risks of property degradation of ferritic and ferritic-martensitic steels.

It is currently expected that nanosized oxide particles in ODS steel should be beneficial for mitigation of both swelling and high temperature embrittlement, providing additional recombination sites for point defects and He trapping sites at the particle/matrix interfaces, thus preventing excessive helium accumulation at the grain boundaries [10,14–19]. However, ODS steels have very complicated microstructure with multiple sinks (grain boundaries, dislocations, second phase precipitates) competing for point defects and helium atoms. The relative role of the additional oxide nanoparticles in the overall material response to helium accumulation is far from obvious. In different ODS steels and at different testing conditions the fraction of helium bubbles affiliated with the nano-oxides is known to vary from 30 to 100% [10,12,15,19–22]. Neither is it evident that the efficient bubble nucleation and growth on the nano-oxides is always safe from promoting bubble-to-void transition in particular irradiation environments [23–25] and thus drastically accelerating swelling onset instead of additionally postponing it. The available literature knowledge remains unsystematic and often badly reproducible due to the lack of a basic understanding of the involved microstructural mechanisms.

In order to clarify the relative contribution to helium accumulation and swelling from the oxide nanoparticles as a part of the complex microstructure of ODS-EUROFER, the impact of all microstructural defects should be estimated quantitatively. To reach this goal, it is important to perform systematic studies of the sensitivity of gas-driven microstructure to the variation of key parameters, which include the nano-oxide sizes and number densities, gas content and processing temperatures. It is highly desirable to perform investigations using as much control over the experimental parameters as possible. From this point of view, the use of the ion implantation technique for the imitation of microstructural changes in well-controlled conditions with a wide range of variable parameters combined with careful post-implantation characterization looks highly promising. It also allows investigating the kinetics of material microstructure development to He accumulated doses well above those expected in the forthcoming reactor designs, providing a reliable basis for long-term predictions of the investigated material behavior.

The major objective of this paper is a systematic investigation of the fundamental trends in helium-driven microstructure development in ferritic-martensitic ODS steels in separate ion implantation experiments with varying single parameters (accumulated gas content, gas accumulation and damage rates, and sample temperature), with particular attention to the role of the oxide particles.

Material and methods

Materials and sample preparation

The EUROFER97 samples originate from the batch E83697 manufactured by Boehler Austria GmbH. The processing route of EUROFER 97 steel includes conventional ladle metallurgy, refining via vacuum arc re-melting, and hot rolling in the austenitic temperature range. ODS-EUROFER was produced using powder metallurgy technique that included mechanical alloying of EUROFER 97 powder with 0.3% yttrium at Plansee GmbH, followed by a hot isostatic pressing (HIP) and a hot cross-rolling at 1150 °C (for details, see Ref. [7]). Before being supplied for the current experiment, both steels were subjected to additional heat treatments. The samples of EUROFER 97 were austenitized for 30 min at 980 °C, quenched in air and then tempered for 2 h at 760 °C, while ODS-EUROFER samples were austenitized at 1100 °C for 30 min, quenched and then tempered at 750 °C for 2 h. These heat-treated samples are referred to below as 'as-supplied samples'. Table 1 summarizes the average elemental content in the samples expected from the measurements on the samples of same steel batch [7,26,27].

Detailed microstructural studies of non-irradiated ODS-EUROFER [15,28–44] and EUROFER 97 [30–33,35,45–47] are already available in the literature; some additional details for as-supplied samples are given in section 3.1 for clarity.

Slices of ODS-EUROFER and EUROFER97 steel with the thickness of $\sim$ 300 μm were cut out from the supplied samples, mechanically grinded down to $\sim$ 100 μm and discs of 3 mm diameter were punched out of the slices. Prior to irradiation, the discs were electropolished in a StruersTenupol-5 unit with a 10% $HClO_4$ + 90% CH_3OH solution at –20 °C in order to remove any damage due to mechanical polishing. After electropolishing, the samples were cleaned from both sides by ion milling system PIPS 693 using a 3 eV ion beam and 5–6° etching angle for 2 min.

Ion implantation conditions

The implantation of investigated steels was performed with 10 keV He ions using IRMA implanter at the JANNuS-Orsay MOSAIC facility of IJCLab [48]. Ion injection was performed in the direction normal to the sample surface. The selection of the He ion energy was motivated by relatively low production of radiation-induced vacancies, suitable region for TEM analysis using standard sample geometry and a homogenous bubble size distribution over helium implantation depth (see section 3.2.1 for more details). According to calculations with the SRIM code [49] in full damage cascade regime, the damage and ion implantation (R_p) peaks for 10 keV He$^+$ ions lie at the depths of 28 and 48 nm, respectively. Because the implantation and damage profiles generated by He ions are not perfectly uniform over the implanted sample depth, it was important to define a specific depth range within which the TEM analysis was to be performed and the relevant concentrations and doses calculated. As described below in section 3.2.1, this range was chosen to span 10 to 40 nm from the initial sample surface in order to obtain ample statistics with a sufficiently high accuracy of bubble size determination and to minimize the influence of the surface.

He$^+$ ion implantation into ODS-EUROFER steel samples was done at different combinations of ion flux, fluence and sample temperature. The particular fluence, flux and temperature values were selected within the ranges of 1×10^{15}-1×10^{16} cm^{-2}, 5×10^{11}-5×10^{12} cm^{-2}s^{-1}, and 293–923 K, respectively. Samples of ODS-EUROFER implanted at room temperature (RT, 293 K) were additionally post-implantation annealed (PIA) during 90 min under vacuum in order to reveal any microstructural features that might be obscured by the low mobility of the implanted ions and implantation-produced primary damage at RT. In order to compare the general trends of ODS-EUROFER steel microstructural evolution under helium implantation with the behavior of oxide-free material, EUROFER 97 steel was implanted with 10 keV He$^+$

Table 1

Chemical composition of ODS- EUROFER and EUROFER97 steels (in wt.%) [7,26,27].

Element	C	Cr	Si	Mn	V	W	Ta	Y	O	Fe
ODS-EUROFER	0.07	8.92	0.11	0.41	0.19	1.11	0.08	0.19	0.14	Balance
EUROFER 97	0.12	8.91	0.04	0.48	0.20	1.08	0.14	–	–	Balance

at 823 K with the flux of 5×10^{11} cm^{-2}s^{-1} up to the fluence of 1×10^{16} cm^{-2}.

The experimental implantation parameters and those calculated by SRIM for various fluence, flux and temperature regimes are summarized in Table 2. The calculated values for the region of interest investigated by TEM (ROI, 10–40 nm from the beam-facing sample surface) are averages over the ROI width. Later on, all mentioned parameters related to the implantation are those estimated for ROI. They are typically around 20% smaller than the values at the peak position depth.

Material characterization and data processing

Prior to the implantations, the samples of ODS-EUROFER and EUROFER97 steels were investigated by scanning electron microscopy (SEM) at Zeiss Evo 50 XVP microscope (NRNU MEPhI) equipped with Nordlys S EBSD detector in order to identify the grain sizes and estimate the density of grain boundaries, the latter being among the critical input parameters required for an implantation-induced swelling estimation. For a better identification of grains in as-supplied ODS-EUROFER steel, where grains are noticeably smaller than in EUROFER97, the electron backscatter diffraction (EBSD) technique [50] was used to image the microstructure of ODS-EUROFER at the grain and sub-grain scales. The EBSD data analysis was done using HKL Channel 5 software.

The sample microstructure was investigated both prior and after ion implantations by transmission electron microscopy carried out using FEI TECNAI G^2 20 Twin microscope (JANNuS-Orsay). For these investigations, the samples were additionally thinned from the unirradiated side to the electron transparency using a Tenupol-5 unit with the same electrolyte and thinning regime as that used prior to ion implantation. Electropolished samples were cleaned from both sides by an ion milling system PIPS Gatan693 using a 1 keV ion beam and 4–5° etching angle for 2 min and then directly used for TEM investigations.

The implanted samples were studied using bright-field transmission electron microscopy (BF TEM) through-focal series method in planar view. In order to estimate the number density of He bubbles formed as a result of the implantation, the local thickness of TEM samples was measured by electron energy loss spectroscopy (EELS) log-ratio approach, which has an uncertainty of $\pm$ 10% [51,52]. Cavity sizes were determined as the diameters of the first Fresnel fringe on a bubble observed in the underfocused image [53,54]. The related uncertainty is within 10%. Other details about TEM data acquisition, estimation of bubble size, bubble density, swelling and accumulated He fraction in bubbles associated with different microstructural features can be found

in Ref. [25].

Results

ODS-EUROFER and EUROFER 97 microstructure in as-supplied state

Microstructure of both ODS-EUROFER and EUROFER 97 steels in as-supplied state is characterized by elongated grains with some carbide precipitation preferentially along the grain boundaries (as illustrated in Fig. S1 in the Supplementary materials). ODS-EUROFER contains also Y_2O_3 nanoparticles visibly uniformly distributed inside the grains (see inset in Fig. S1(c)). ODS-EUROFER steel has noticeably a finer grain structure than EUROFER 97. Smaller grains in ODS-EUROFER steel form because of finely-dispersed Y_2O_3 nanoparticles that provide strong pinning effects on austenite grain growth during steel austenitization [31,35]. No retained austenite was present in both steels in as-supplied state [31,34].

The as-supplied EUROFER 97 steel has a fully tempered martensitic structure with martensite laths, blocks and packets within prior austenite grains, in agreement with Refs. [30,31,45,46]. An average size of martensite laths in EUROFER 97 is about 0.8–6.5 μm length and 0.3–0.5 μm width; the typical prior austenite grain size is 8–9.4 μm. The absence of residual ferrite in ODS-EUROFER steel with 0.3 wt% of Y_2O_3 is in agreement with the results of Ref. [55] that show a fully martensitic structure in 9Cr ODS steels with the weight content of Y_2O_3 below certain limit. Though we did not pursue a detailed search for the presence of residual ferrite, the results of Ref. [34] obtained on the same material assure us that ODS-EUROFER used in this study has essentially a tempered martensitic microstructure.

The as-supplied ODS-EUROFER steel was found to have a weak crystallographic texture, as could be expected for hot-rolled steels following martensitic transformation. Grains with irregular morphology were sometimes found. According to the results of EBSD mapping (see Fig. S2 in the Supplementary materials), high-angle grain boundaries (HAGBs) with grain misorientation angles $\geq$ 15° dominate, though low angle grain boundaries (LAGBs) with misorientations between 2° and 15° were also present at a lower share of $\sim$ 24% (see Fig. S2(c)). The dislocation wall boundaries with misorientations below 2°, even if present, cannot be properly indexed by SEM EBSD.

Two peaks at $\sim$ 2° and 59° could be seen in the grain misorientation distribution histogram obtained from the mesotexture EBSD data (see Fig. S2(d) in the Supplementary materials). A similar distribution was reported earlier for quenched [31] and quenched/tempered [35,44]

Table 2

Summary of parameters used for implantations with 10 keV He$^+$ ions.

Parameters	Fluence variation runs			Flux variation runs		Temperature variation runs		
Flux, 10^{11} cm^{-2}s^{-1}	5.0	5.0	5.0	10.0	50.0	10.0	5.0	5.0
Fluence, 10^{15}cm^{-2}	1.0	5.0	10.0	5.0	5.0	5.0	5.0	5.0
T, K	823	823	823	823	823	293 + PIA at 823	723	923
Peak dose rate, 10^{-5}dpa/s	3.90	3.90	3.90	7.80	39.0	7.80	3.90	3.90
ROI dose rate, 10^{-5}dpa/s	3.63	3.63	3.63	7.27	36.3	7.27	3.63	3.63
Peak dose, dpa	0.08	0.39	0.78	0.39	0.39	0.39	0.39	0.39
ROI dose, dpa	0.07	0.36	0.73	0.36	0.36	0.36	0.36	0.36
Peak He accumulation rate, appm/s	0.85	0.85	0.85	1.70	8.48	1.70	0.85	0.85
ROI He accumulation rate, appm/s	0.63	0.63	0.63	1.25	6.27	1.25	0.63	0.63
Peak He concentration, 10^3appm	1.70	8.48	16.95	8.48	8.48	8.48	8.48	8.48
ROI He concentration, 10^3appm	1.25	6.27	12.53	6.27	6.27	6.27	6.27	6.27
ROI appm/dpa ratio, 10^4	1.72	1.72	1.72	1.72	1.72	1.72	1.72	1.72

ODS-EUROFER steel. According to Ref. [31], the maximum at $\sim 2°$ is presumably related to lath boundaries or dislocation substructures, while the maximum at $\sim 60°$ is related to the crystallographic nature of the martensitic transformation itself (selection variants) and corresponds to packet or/and block boundaries. The average grain size in as-supplied ODS-EUROFER steel measured over 500 grains is found to be $\sim 0.7 \times 0.32$ μm. Although rare coarser grain regions (not shown) similar to those reported in Ref. [34] were detected on SEM EBSD maps, these regions were not met on TEM images in the zones where the He bubble parameters were evaluated.

The dislocation densities required for the estimation of the swelling and He inventory due to the dislocation-associated bubbles were borrowed from the literature sources reporting the results of detailed dislocation density evaluation in ODS-EUROFER and EUROFER 97 samples produced in similar conditions. According to the literature data, dislocation density in ODS-EUROFER is by up to a factor of two higher than in EUROFER 97, but is still quite moderate due to a static recovery during the tempering treatment [29,32,37].

The grain boundary inclusions with a globular shape and average size of ~ 100 nm detected in both ODS-EUROFER and EUROFER97 were $M_{23}C_6$ type precipitates rich in Cr, Fe and W in agreement with earlier observations [34,42,45,46]. According to the literature data, the volume density of $M_{23}C_6$ carbides in ODS-EUROFER steels is only half of that in its non-ODS counterpart, possibly due to the lower carbon content. MX (TaC and VN) carbonitride particles with an average size of ~ 20 nm were found inside grains of EUROFER 97, while for ODS-EUROFER the presence of such particles has not been reported [31,35,37].

Numerous dispersed Y_2O_3 particles with typical diameters ranging from 3 to 40 nm were observed in ODS-EUROFER mostly inside the grains. The spatial particle distribution was relatively uniform over individual grains (cf. inset in Fig. S1(c) in the Supplementary materials). However, variations of the particle number density from grain to grain and from one TEM sample to another were noticed. The statistical analysis of ~ 1000 particles on different TEM samples gave an average particle diameter of ~ 12 nm, in good agreement with the literature data [30,32,40,42].

Literature sources (e.g. [15,32,33,38,43]) report strongly different number densities of Y_2O_3 nanoparticles, varying from 5×10^{21} m^{-3} to $\sim 1 \times 10^{23}$ m^{-3} even for the same batch of ODS-EUROFER. In what follows, the oxide particle number density of 1×10^{22} m^{-3} was assumed for the evaluation of the oxide-associated He bubble number density, swelling and He fraction.

Typical microstructural parameters of ODS-EUROFER and EUROFER 97 steels in as-supplied condition are summarized and compared with the known literature data in Table 3. The surface areas of grain boundaries and carbide precipitates per unit ODS-EUROFER volume were calculated using the parameters obtained by SEM EBSD and TEM investigations and assuming that both microstructural features had an ellipsoidal shape.

Microstructure development in ODS-EUROFER steel during helium implantation

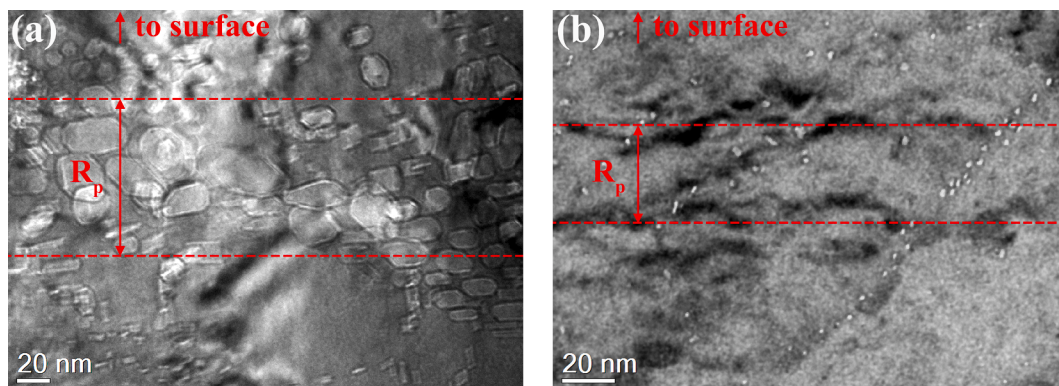*General description of microstructural evolution in ODS-EUROFER*

Distribution of cavities over implantation depth. The evaluation of the observed helium bubble parameters was mostly done in this study using planar view TEM samples. The approach assumes that the size distribution of the bubbles is relatively uniform over the whole sample depth. If the size variation turns out to be pronounced, the interpretation of planar view TEM images becomes quite uncertain. In order to avoid the problem, the incident ion energies and sample thickness should be appropriately selected. This section describes the results of the verification test of the bubble size distribution uniformity with respect to ion stopping profile for implantation runs with 10 and 40 keV He ions. In order to follow the depth variation of cavity sizes, cross-sectional FIB lift-out samples were used in this case.

Fig. 1 compares the results for two different implantations, one with 10 keV to the fluence of 5×10^{15} cm^{-2} at 823 K and another with 40 keV He ions to the fluence of 5×10^{16} cm^{-2} at 923 K. Bright Field TEM (BF TEM) underfocused images are taken from the zone located near the relevant projected ranges, R_p, of He ions.

The implantation with 40 keV He ions results in a non-uniform distribution in both bubble density and size as a function of the depth from the implanted surface (Fig. 1(a)). The largest bubble sizes are observed in the zone corresponding to the projected range R_p of He ions. In contrast, the implantation with 10 keV helium ions results in a relatively uniform bubble distribution as a function of the depth, leading to no preferential bubble growth at the He projection range (see Fig. 1(b)). Therefore, such ion energy is more suitable for the investigations of the He effects expected in the bulk of ODS-EUROFER steel under neutron irradiation because the parameters of He bubble ensembles are sensitive to the microstructural defect distribution rather than to the ion/vacancy ratio variations along the implantation profile. Hence, the He ion energy was selected equal to 10 keV for all implantations in this study.

In order to confirm the relative uniformity of the bubble distribution in the 10 keV He implanted samples, a more detailed analysis was performed. TEM micrographs of ODS-EUROFER steel after ion implantation with 10 keV He ion beam are shown in Fig. 2. The ensembles of He bubbles could be clearly identified by the characteristic change in Fresnel contrast from the overfocus to underfocus conditions.

He bubbles appear at depths from 5–7 to 100 nm from the implanted sample surface. A narrow denuded zone with a thickness of ~ 5 nm was observed in the near surface region. Also, the formation of a $\sim 2–5$ nm thick surface oxide layer was detected. The maximum depth of the He bubble band correlates well with the helium ion stopping and defect production profiles predicted by SRIM based calculation. The He bubble distribution in the implanted volume is heterogeneous; many bubbles clearly decorate microstructural defects - grain boundaries, dislocations

Table 3
Typical microstructural parameters of ODS-EUROFER and EUROFER steels in as-supplied state.

Microstructural component		ODS-EUROFER	Ref.	EUROFER 97	Ref.
Grain boundaries	Mean grain length (10^{-6} m)	0.70	This study	8–9.4	[45,46]
				0.8–6.5[**]	This study
	Mean grain width (10^{-6} m)	0.32	This study	-[**]	[45,46]
				0.3–0.50[**]	This study
	Volume density (10^6 m^{-1})	7.7	This study	not calculated	–
Dislocations	Density (10^{14} m^{-2})	1.3–1.80	[30,31,32]	0.90	[30]
Carbides $M_{23}C_6$	Mean diameter (10^{-6} m)	1.10	This study	1.00	[45,46]
	Number density (10^{19} m^{-3})	0.8–2.70	[34,42]	4.18	[45]
	Volume density (10^5 m^{-1})	9.2	This study	not calculated	–
Y_2O_3 nano-oxides	Mean diameter (10^{-9} m)	12.00	[34]	–	–
	Number Density (10^{21} m^{-3})	10.00	[42]	–	–
MX precipitates	Mean Diameter (10^{-9} m)	–	–	20.00	[45,46]
	Number Density (10^{21} m^{-3})	–	–	1.00	[45–47]

[**] -martensite laths.

Fig. 1. FIB cross-section of ODS-EUROFER steel implanted with (a) 40 keV He ions (fluence 5×10^{16} cm^{-2}, 923 K) and (b) 10 keV He ions (fluence 5×10^{15} cm^{-2}, 823 K). BF TEM imaging conditions: ~1 μm underfocus. Dash lines limit projected range zone (with the highest He content).
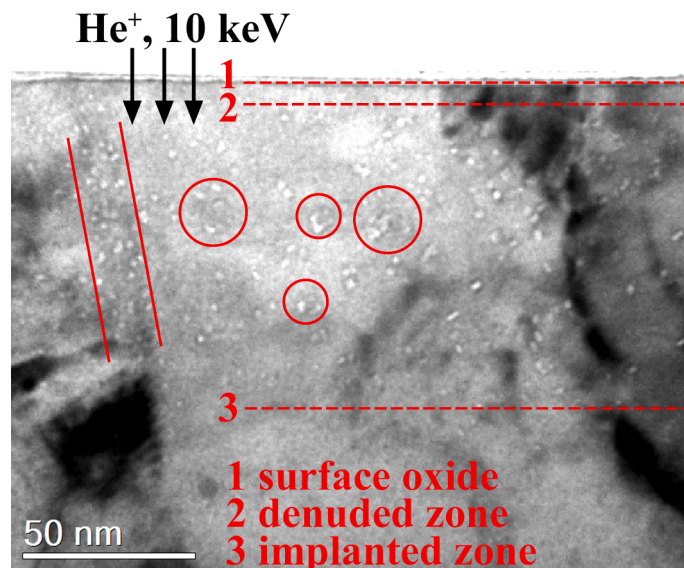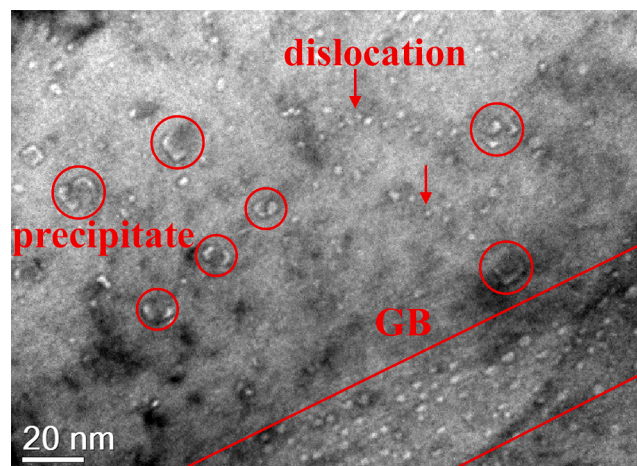

Fig. 2. FIB cross-section of ODS-EUROFER steel implanted with 10 keV He ions (fluence 5×10^{15} cm^{-2}, 823 K). BF TEM imaging conditions: ~1 μm underfocus. Dash lines limit the described zones, solid lines and circles mark structural defects decorated with He bubbles.

and precipitates.

A statistical analysis of the He bubble number density and mean size dependence on the distance from the ion-implanted sample surface (cf. Fig. S3 in the Supplementary materials) has demonstrated that the mean bubble size is practically insensitive to the observation depth and equals to ~ 4.4 ± 0.3 nm, showing no correlation to the helium implantation and vacancy production profiles along the whole ion implanted range. In contrast, the bubble number density follows ion/vacancy generation profile predicted by SRIM. The highest bubble density of $(1.6 \pm 0.2) \times 10^{23}$ m^{-3} appeared at the depths of 20–40 nm from the implanted surface. The depth uniformity of the bubble size distribution justifies the use of planar view observations in order to estimate the spatial distribution of bubbles using the whole surface of implanted sample visible in planar-view TEM.

Fig. 3 shows typical BF TEM images obtained from planar view on a sample of ODS-EUROFER implanted in the same regime as the FIB cross-sectional sample in Fig. 1(b).

The general trend in bubble spatial distribution is similar to that visible on the cross-sectional samples; bubbles decorate grain boundaries, dislocations and precipitates. The overall number of bubbles visible in a single TEM image is, however, notably larger because now there are no restrictions by the narrow thickness (~100 nm) of the ion implantation zone in FIB samples. Also, the quality of images is better

Fig. 3. Planar view of the sample of ODS-EUROFER steel implanted with 10 keV He ions (fluence 5×10^{15} cm^{-2}, 823 K). Sample thickness is ~ 40 nm. BF TEM imaging conditions: ~ 1 μm underfocus.

due to the absence of a thin amorphous layer which is always present at the surface of FIB prepared samples.

Distribution of bubbles over various types of microstructural defects. Having in mind the observations reported in section 3.2.1, several major types of microstructural defects may act as trapping sites for He atoms and serve as nucleation sites for bubble formation in ODS-EUROFER steel, namely high- and low-angle grain boundaries, dislocations, $M_{23}C_6$ and Y_2O_3 precipitates. All TEM data described in this section are obtained in the same experimental conditions, namely 10 keV He ion implantation to the fluence of 5×10^{15} cm^{-2} with the flux of 5×10^{11} cm^{-2}s^{-1} at 823 K.

Fig. 4 shows typical BF TEM images for areas containing dislocations and either a high-angle grain boundary, see Fig. 4(a)), or a low-angle grain boundary, see Fig. 4(b).

It is clearly seen that the helium readily accumulates in small He bubbles with a high number density at both types of grain boundaries and at dislocations. Low-angle grain boundaries in ODS-EUROFER (see Fig. 4(b)) appear to be dislocation walls. Hence, for the bubble number density and swelling estimations, only high-angle grain boundaries were considered. Since low-angle grain boundaries are decorated with the bubbles similar to dislocations, they are not treated explicitly during the subsequent statistical analysis because the density of dislocations contained in low-angle grain boundaries is two orders of magnitude lower than the dislocation density inside the grain bulk. The typical sizes of He bubbles associated with both types of grain boundaries are similar to sizes of bubbles at dislocations and bubbles within the grain bulk (i.e. those not associated with any extended defect or precipitate/particle). In contrast to austenitic steels, where helium bubbles at grain boundaries at the studied temperature tend to coalesce and promote high-temperature helium embrittlement [4], we have noticed no bubble coalescence at the grain boundaries in ODS-EUROFER. Preliminary TEM examinations indicate that in the discussed regime the number density of bubbles in the bulk is low.

Typical BF TEM micrographs of a globular $M_{23}C_6$ carbide precipitate (~100 nm in diameter) at the grain boundary and several Y_2O_3 nano-oxide precipitates (~7–30 nm in diameter) in the grain bulk of ODS-EUROFER sample are shown in Fig. 5(a) and 5(b), respectively. As can be seen in Fig. 5(a), at the $M_{23}C_6$ precipitate/matrix interface the implanted helium promotes the formation of multiple relatively small equiaxial (spherical or faceted) He bubbles, slightly smaller than those in the surrounding matrix. In contrast, the Y_2O_3 nanoparticles host in the same implantation conditions single (rarely two) relatively large bubbles with notably larger size than the typical size of bubbles in the matrix

(see Fig. 5(b)). The helium bubbles attached to Y_2O_3 particles have specific lens-like shapes. Quite evidently, helium in ODS-EUROFER steel behaves differently at the yttria/matrix and carbide/matrix interfaces.

All the observed Y_2O_3 nanoparticles, regardless of their size, hosted He bubbles. A definite correlation of the bubble sizes with the sizes of the host oxide particles could be noticed; with the increase of the nanoparticle size, the size of attached bubble increased as well (cf. Fig S4 in the Supplementary materials). Similarly, in Ref. [56] practically all the oxide nanoparticles were also decorated with He bubbles. It should be kept in mind, however, that bubble to oxide association is not a universal law. For example, in very different implantation conditions the share of particles covered with bubbles could be as low as 30–40% [19] or there could be no particles covered with bubbles at all [13,57].

The relative importance of different defect microstructure components for He accumulation depending on ion implantation parameters

The estimation of material swelling based on TEM data requires the knowledge of the bubble volumes and number densities (i.e. the number of bubbles per unit volume). These parameters in the case of He implantation depend on both the He ion implantation parameters used, and the densities of microstructural defects that promote the He bubble formation. Hence, the He bubble distributions at all microstructural features, as well as in the bulk of the grains, were characterized as a function of the He ion implantation fluence, flux and temperature.

Fluence variation effect on bubble parameters, contributions to swelling and helium inventory in different bubble families. In order to systematically study the effect of various experimental parameters on the kinetics of bubble ensembles in ODS-EUROFER, several series of experiments were performed, where only one of the implantation parameters was changed with the others being kept fixed. This section discusses the bubble evolution in samples implanted with He at 823 K to fluences 1×10^{15} cm^{-2}, 5×10^{15} cm^{-2}, and 1×10^{16} cm^{-2} at the constant flux of 5×10^{11} cm^{-2}s^{-1}. The accumulated He concentrations at these fluences are cited in Table 2.

For all three fluences, the partitioning of implanted He between different microstructural defects and the bulk is observed (see typical TEM images of ODS-EUROFER samples in Fig. S5 in the Supplementary materials): He bubbles decorate grain boundaries, dislocations and precipitates. As can be seen, with the increase of the helium implantation fluence the size of the bubbles also increases.

The shape of He bubbles changes from more rounded at the lowest fluence to faceted at higher fluences, which is common for both voids
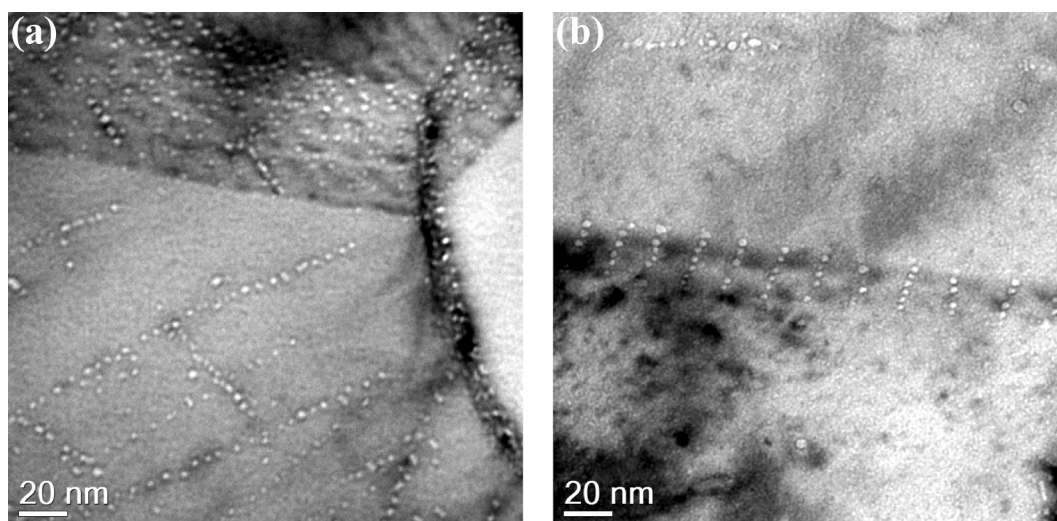

Fig. 4. The images of high-angle grain boundaries and dislocations (a) and low-angle grain boundaries and dislocations (b) in ODS-EUROFER steel implanted with 10 keV He ions (fluence 5×10^{15} cm^{-2}, flux 5×10^{11} cm^{-2}s^{-1}, 823 K). BF TEM imaging conditions are: ~ 0.5 μm underfocus.
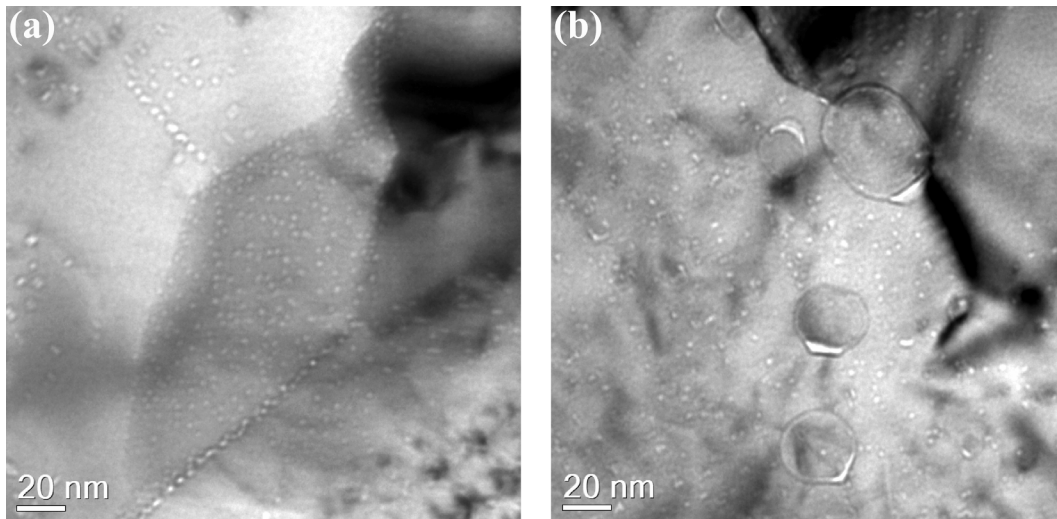
Fig. 5. Typical images of $M_{23}C_6$ carbide precipitates (a) and Y_2O_3 nanosized precipitates (b) in ODS-EUROFER steel implanted with 10 keV He ions (fluence 5×10^{15} cm^{-2}, flux 5×10^{11} cm^{-2}s^{-1}, 823 K). BF TEM imaging conditions: ~ 0.5 μm underfocus.

and He bubbles in bcc Fe and Fe-Cr alloys [58,59]. Typical faceted cavities obtained at the highest fluence of 1×10^{16} cm^{-2} are shown in Fig. 6.

A characteristic feature of the bubble microstructure at all three fluences is the remarkably larger size of bubbles associated with oxide particles as compared to the bubbles associated with other microstructural defects or the bubbles in the bulk. At the highest fluence, the bubbles attached to oxide particles often reach sizes similar to or even larger than the size of the host particle itself (see Fig. 7). As a result, the particles smaller than approximately 10 nm are largely enveloped by the bubbles, leaving only a minor neck connecting particle to the matrix. A similar effect was met also at lower studied fluences, but the fraction of particles 'swallowed' by bubbles was relatively small.

In order to describe the variation of the bubble parameters with the increase of the fluence in quantitative terms, we start with the bubbles
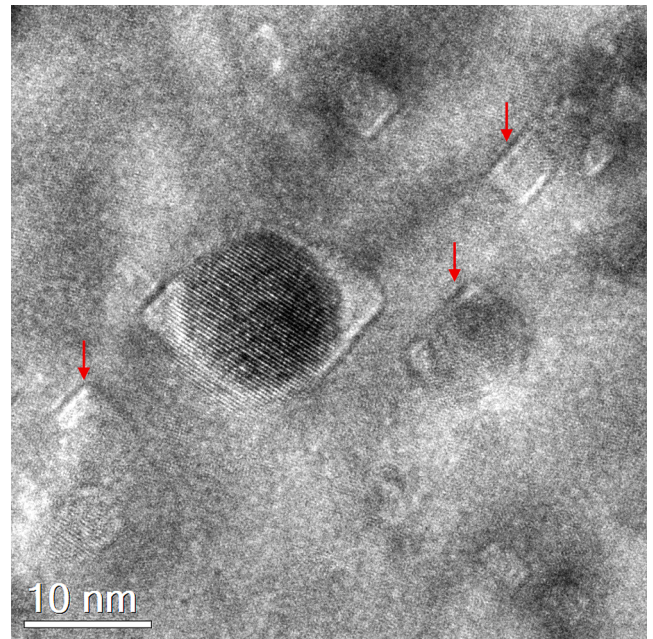

Fig. 7. Association of He bubbles with Y_2O_3 nanoparticles of different size in ODS-EUROFER steel implanted with 10 keV He ions to the fluence of 1×10^{16} cm^{-2} (flux 5×10^{11} cm^{-2}s^{-1}, 823 K). Oxide particles nearly completely enveloped by He bubbles are marked by arrows. BF TEM imaging conditions: ~0.4 μm underfocus.
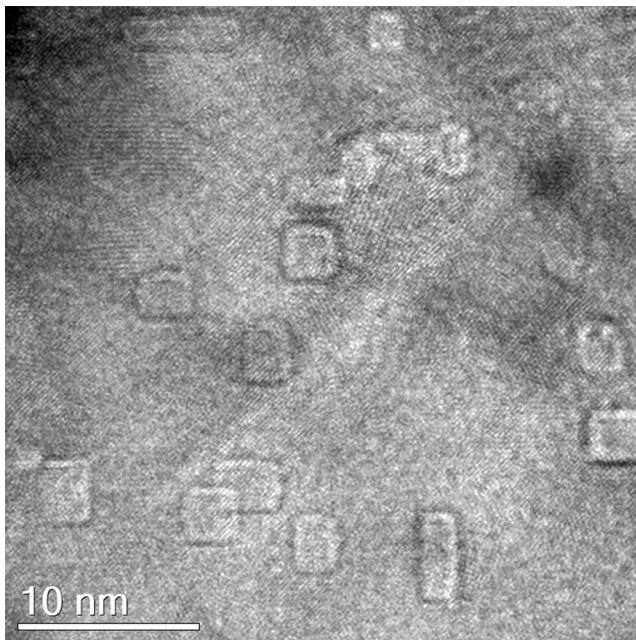

Fig. 6. He bubbles inside the grains of ODS-EUROFER steel implanted with 10 keV He ions to the fluence of 1×10^{16} cm^{-2} (flux 5×10^{11} cm^{-2}s^{-1}, 823 K). BF TEM imaging conditions: ~0.4 μm underfocus.

associated with oxide nanoparticles that require a special treatment due to both their specific lens shape and dependence on host particle size. Following the procedure described in our earlier publication [25], here and below we evaluate the average size of oxide-associated cavities, $\langle D_c^p \rangle$, as the size of the bubbles associated with the particles of the average size over the particle population (i.e. 12 nm in our case). In order to determine the relevant average bubble size, we employ the trend curves for bubble diameters D_c^p as a function of particle diameter D_p obtained by fitting the experimental points for the observed bubble sizes, as shown in Fig. 8.

The observed correlation between the diameters of the bubbles on oxide particles and the sizes of their host particles for the case of an implantation fluence variation is shown in Fig. 8(a). At all three fluences
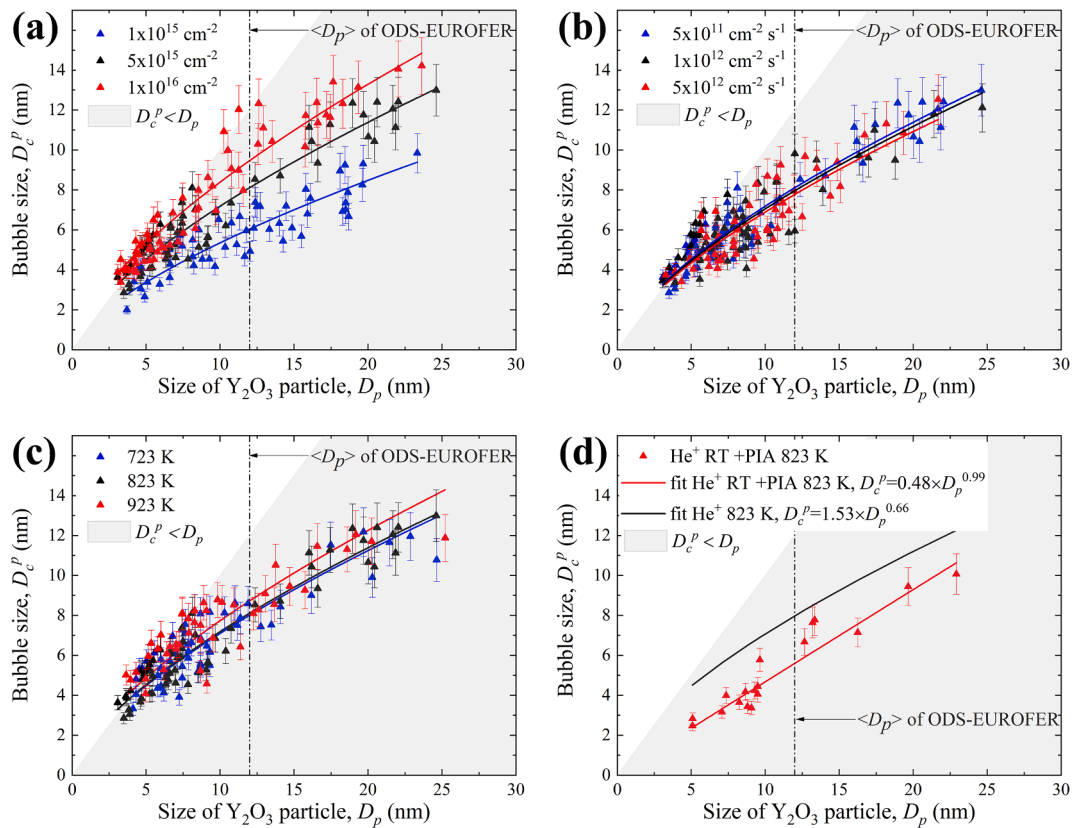
Fig. 8. The observed bubble sizes on yttria nanoparticles vs. the nanoparticle size for the ODS-EUROFER steel samples implanted with 10 keV He ions in different implantation conditions (a-c) or processed in the RT + PIA regime (d). Solid lines are the best fits for each particular combination of fluence, flux and temperature. (a) Variation of the fluence between 1×10^{15} and 1×10^{16} cm^{-2} at the flux of 5×10^{11} cm^{-2}s^{-1} and 823 K. (b) Variation of the flux from 5×10^{11} to 5×10^{12} cm^{-2} s^{-1} at the fluence of 5×10^{15} cm^{-2} and 823 K. (c) Variation of the temperature from 723 to 923 K for the fluence of 5×10^{15} cm^{-2} at the flux of 5×10^{11} cm^{-2}s^{-1}. (d) The red line is the fit for the RT + PIA data, as described in the legend. For comparison, the black line shows a similar fit obtained earlier for the relevant high-temperature He implantation, cf. Fig. 8(b). The areas marked in all panels with a grey background correspond to the bubbles with the size smaller than that of the host particle. The parameters of the fitting curves for panels (a-c) can be found in Table S1 in the Supplementary materials. (For interpretation of the references to color in this figure legend, the reader is referred to the web version of this article.)

one can see clear trends that can be conveniently fitted with a power law, $D_c^p = aD_p^b$. The effective average diameters of the bubbles on oxide particles determined using the derived trend lines are found to be 6.0 nm, 8.1 nm, and 9.5 nm for the helium ion fluences 1×10^{15} cm^{-2}, 5×10^{15} cm^{-2}, and 1×10^{16} cm^{-2}, respectively. At the same time, within a fixed fluence, $\langle D_c^p \rangle$ increases as the nanoparticle size increases, for instance from 4 nm to 14 nm with the nanoparticle size increase from 3 to 23 nm at the fluence of 1×10^{16} cm^{-2}. In other words, the average size of bubbles associated with yttria nanoparticles only weakly depends on the He fluence in the studied range and is mostly affected by the size of the host nanoparticles. Already at the intermediate fluence one can notice some particles with sizes close to 5 nm that host bubbles of comparable or larger size (falling in the white background zone in Fig. 8 (a)). At the highest fluence value of 1×10^{16} cm^{-2} the relation $D_c^p \gtrsim D_p$ is commonly met for smaller (less then, roughly, 7 nm) particles, but sometimes the bubbles envelope particles as large as 12 nm in diameter.

The average bubble size D_c^p, number density N_V^k, swelling contribution S_k, the estimated average ratio of vacancies to He atom number in the bubbles (V/He), and the fraction of accumulated helium F_{He}^k were calculated separately for each bubble family (at grain boundaries, dislocations, carbides, oxides and in the grain interior) for all three studied fluencies following the approach described in detail in Ref. [25]. The results are summarized in Table 4.

As can be concluded from the data in Table 4, at each particular fluence there is little difference in size between the bubbles in the bulk and the bubbles on dislocations and grain boundaries, the latter being

only ~ 10% larger than the others. The bubbles on carbides are typically somewhat smaller, while those on oxide particles are noticeably larger. The increase of the ion implantation fluence and the total content of the implanted He in the matrix leads to the growth of all bubble types, including those in the bulk and on all microstructural features. The largest size increase (by a factor of ~ 2) between the fluences of 1×10^{15} and 1×10^{16} cm^{-2} was observed for the bubbles at grain boundaries and in the grain matrix. Slightly slower growth, by a factor of 1.8, was detected for the bubbles on dislocations. Both types of precipitates, i.e. $M_{23}C_6$ carbides and Y_2O_3 oxides, promote the lowest bubble growth rate.

The fluence dependent variations of the bubble number densities are also sensitive to the nature of the bubble family. The most favorable location for the bubbles at all fluences is on the grain boundaries. The evaluated bubble number density at the grain boundaries increases with fluence, but quite moderately. Even less pronounced dynamics of number density is demonstrated by the bubble families associated with the other extended defects - dislocations and carbide precipitates. The number density of bubbles associated with oxide nanoparticles is uniquely determined by the number density of nanoparticles, $N_V^p = 1.0 \times 10^{22}$ m^{-3}, and also does not change as the fluence increases. In contrast, the number density of bubbles in the bulk continuously grows. While at the lowest studied fluence it is comparable to that of bubbles on dislocations and carbides, by the highest accumulated He fluence it becomes essentially the same as that of grain boundary bubbles. But in spite of the sharp increase of the number density of bubbles in the bulk, the total bubble number density grows with the implantation fluence

Table 4

Mean sizes and number densities of cavities associated with different microstructural features and their contributions to swelling, V/He ratio and the accumulated He fraction in ODS-EUROFER implanted with 10 keV He$^+$ ions to different fluences.

1×10^{15} cm^{-2}	D_c^k (10^{-9} m)	N_V^k (10^{22} m^{-3})	S_k (%)	V/He$_k$	F_{He}^k (10^3 appm)	F_{He}^k (%)
Grain boundaries	3.04 ± 0.23	3.64 ± 0.75	0.053 ± 0.013	1.52	0.36 ± 0.09	28.3 ± 7.0
Dislocations	2.80 ± 0.17	1.95 ± 0.24	0.022 ± 0.004	1.47	0.15 ± 0.03	12.2 ± 2.0
Carbides	2.72 ± 0.27	1.84 ± 0.18	0.019 ± 0.006	1.46	0.13 ± 0.04	10.7 ± 3.4
Y$_2$O$_3$	6.04 ± 0.60	1.00 ± 0.10	0.028 ± 0.009	2.03	0.14 ± 0.04	11.2 ± 3.5
Grain bulk	2.68 ± 0.20	1.92 ± 0.22	0.019 ± 0.003	1.45	0.13 ± 0.02	10.7 ± 1.9
Total		10.35 ± 2.12	0.143 ± 0.045		0.92 ± 0.29	73.1 ± 23.1
5×10^{15} cm^{-2}	D_c^k (10^{-9} m)	N_V^k (10^{22} m^{-3})	S_k (%)	V/He$_k$	F_{He}^k (10^3 appm)	F_{He}^k (%)
Grain boundaries	4.79 ± 0.35	5.32 ± 1.44	0.31 ± 0.09	1.83	1.69 ± 0.47	26.9 ± 7.6
Dislocations	4.69 ± 0.24	2.00 ± 0.23	0.11 ± 0.01	1.81	0.60 ± 0.079	9.6 ± 1.1
Carbides	3.55 ± 0.36	2.13 ± 0.21	0.05 ± 0.02	1.61	0.31 ± 0.10	5.0 ± 1.6
Y$_2$O$_3$	8.11 ± 0.81	1.00 ± 0.10	0.10 ± 0.03	2.35	0.42 ± 13	6.7 ± 2.1
Grain bulk	4.36 ± 0.23	2.81 ± 0.46	0.12 ± 0.02	1.76	0.70 ± 0.12	11.2 ± 1.8
Total		13.26 ± 3.59	0.68 ± 0.22		3.72 ± 1.18	59.4 ± 18.8
1×10^{16} cm^{-2}	D_c^k (10^{-9} m)	N_V^k (10^{22} m^{-3})	S_k (%)	V/He$_k$	F_{He}^k (10^3 appm)	F_{He}^k (%)
Grain boundaries	6.05 ± 0.53	5.45 ± 0.59	0.63 ± 0.09	2.03	3.13 ± 0.42	25.0 ± 3.4
Dislocations	5.23 ± 0.56	2.00 ± 0.20	0.15 ± 0.03	1.90	0.79 ± 0.15	6.3 ± 1.2
Carbides	3.96 ± 0.40	2.21 ± 0.22	0.07 ± 0.02	1.69	0.43 ± 0.14	3.4 ± 1.1
Y$_2$O$_3$	9.46 ± 0.95	1.00 ± 0.10	0.19 ± 0.06	2.55	0.76 ± 0.24	6.0 ± 1.9
Grain bulk	5.37 ± 0.75	5.40 ± 1.24	0.44 ± 0.15	1.92	0.23 ± 0.79	18.3 ± 6.3
Total		16.06 ± 3.68	1.48 ± 0.49		7.40 ± 2.34	59.0 ± 18.7

relatively modestly, from $N_V \approx 1.0 \times 10^{23}$ m^{-3} up to $N_V \approx 1.6 \times 10^{23}$ m^{-3}.

The overall increase of the number densities of visible He bubbles with the increasing fluence is accompanied with the increase of swelling, but the contributions to swelling vary depending on the particular bubble family. The largest contribution for all fluences comes from the grain boundary bubbles. However, in terms of swelling rate, the most notable swelling increase (by more than a factor of 20) is provided by the bubble population in the bulk. Individual swelling contributions of bubble populations attached to other extended defects and oxide nanoparticles are smaller than that of grain boundary bubbles and demonstrate slower dynamics (increasing by a factor of ~ 6 for the bubbles on dislocations and oxide particles, and ~ 3.5 for the bubbles on carbides).

The total swelling due to all visible bubbles shows nearly linear variation with the fluence. However, in addition to helium accumulated in the bubbles visible in the TEM images, a certain fraction of implanted helium can be retained in He-vacancy clusters that are too small to be visible; it also contributes to swelling. Hence, an important parameter to estimate is the fraction of implanted He that is captured in the visible bubbles at different fluences. It can be expected that with the growth of bubbles during ion implantation the relative content of He captured in them (per unit sample volume) would decrease. A convenient measure of this effect is the ratio of the number of vacancies contained in a bubble to the number of He atoms it contains, or the V/He ratio. It can be noticed in Table 4 that the estimated V/He ratio indeed increases with the fluence for all bubble families. The lowest He contents are obtained for the bubbles attached to the oxide nanoparticles, which are generally larger than the bubbles in the bulk or on extended defects.

The largest estimated fraction of accumulated helium at the lowest studied fluence is captured in the grain boundary bubble population. The fluence increase up to 1×10^{16} cm^{-2} leads to noticeable increase of the implanted He share accumulated in the bubbles in the bulk and causes only a slight decrease of helium fraction in the bubbles on grain boundaries. So, despite the decrease, the grain boundary cavities remain the most important accumulators of implanted helium. At the same time, the shares of He accumulated in the bubbles on dislocations, carbides, and nano-oxides significantly decrease at the highest implantation fluence.

The cumulative helium fraction captured in all visible bubbles, when expressed in absolute numbers, increases from ~ 920 appm to ~ 7400 appm when the implantation fluence increases from the lowest to the highest accumulated value. However, the fraction of total implanted helium that is trapped in visible bubbles of all types demonstrates the decrease from ~ 73% down to ~ 60% with the fluence increase. In other words, a very noticeable fraction of the implanted He atoms in this experiment remains dissolved in the matrix, presumably being trapped in vacancies and small vacancy clusters that cannot be resolved by TEM or, to some extent, in the yttria particles that, according to Ref. [60], can efficiently accommodate He atoms.

Flux variation effect on bubble parameters, contributions to swelling and helium inventory in different bubble families. Another series of implantation runs was performed at the same temperature of 823 K in order to clarify the sensitivity of the evolving bubble ensembles to the rate of helium introduction into the steel matrix. For this purpose, He ion implantations with three different fluxes, 5×10^{11}, 1×10^{12}, and 5×10^{12} cm^{-2}s^{-1}, were performed to achieve the same fluence of 5×10^{15} cm^{-2}, corresponding to the total accumulated He concentration of ~ 6.3×10^3 appm.

A helium bubble partitioning between the bulk and the microstructural defects in ODS-EUROFER steel was observed for all studied flux values (typical BF TEM images of samples implanted using different fluxes are shown in Fig. S6 in the Supplementary materials).

In order to quantify the trends in the bubble parameter changes with the variation of the implantation flux, TEM observations have been processed as described in section 3.2.2.1. Let us start again with the bubbles attached to the Y$_2$O$_3$ nanoparticles. For all fluxes used one observes correlation between the sizes of the bubbles and those of the host nanoparticles. In order to estimate the average bubble size, the trend lines $D_c^p(D_p)$ were determined for each flux from the plot of bubble size versus host particle size, as shown in Fig. 8(b).

As can be seen, the trend lines indicate only a slight decrease of the bubble sizes on oxide particles when the flux increases by an order of magnitude, while $\langle D_c^p \rangle$ remains almost unchanged. The effective average diameters of the bubbles on oxide particles determined using the derived trend lines are found to be 8.1 nm, 8.0 nm, and 7.8 nm for the helium ion fluxes of 5×10^{11}, 1×10^{12}, and 5×10^{12} cm^{-2}s^{-1}, respectively. For all fluxes used, one can notice oxide particles with bubbles larger than the particle itself. Such oxide particles fall in the size range of 3 to $\sim$ 7 nm and this range is not sensitive to the flux variation, in contrast to the case of fluence variation.

Table 5 summarizes the measured bubble parameters and estimated contributions to swelling, V/H ratio and He inventory separately for each bubble family at three different fluxes.

The parameters of bubbles on $M_{23}C_6$ carbide particles could not be determined at the fluxes of 1×10^{12} and 5×10^{12} cm^{-2}s^{-1} because electron transparent zones in these samples contained no carbides. However, for the purpose of a subsequent comparison of contributions to swelling from the bubbles on different defects, one can roughly estimate them using the knowledge acquired during the implantations with different fluences described in the previous section.

In particular, the specific number density of bubbles (per unit surface of carbide particles) practically saturates by a fluence of 5×10^{15} cm^{-2}, while the average size of the bubbles on carbides, D_c^c, correlates with the average size of the bubbles in the bulk. Hence for swelling estimates at different fluxes we assume the same specific number density of bubbles on the carbide surface, $N_c^c = 2.3$ m^{-2}, while the bubble diameters for the fluxes in the range $1 \times 10^{12} - 5 \times 10^{12}$ cm^{-2}s^{-1} are estimated from the diameters of the bubbles in the grain matrix, D_c^V, using the relation:

$$D_c^c = A D_c^V \tag{1}$$

where A is the ratio of corresponding average bubble diameters at the flux of 5×10^{12} cm^{-2}s^{-1}, for which carbides were observed. Corresponding estimates are also added to Table 5. Finally, the data for the bubbles on oxide particles, as estimated above, is added to Table 5 for completeness.

As can be judged from Table 5, at each particular flux there is little difference between the average sizes of the bubbles in the bulk and on the extended defects. Similarly, whatever the flux, the bubbles associated with Y_2O_3 nano-particles are the largest ones.

A common trend for the bubbles in the bulk, on the dislocations and at the grain boundaries is the increase of the bubble specific number

density $\langle N_c^k \rangle$ accompanied with the decrease of the average bubble size D_c^k as the implantation flux grows. The most impressive number density increase (by a factor of more than 7) between the lowest and the highest implantation flux used is observed for the bubbles in the grain matrix. The increase of the specific bubble number densities at grain boundaries and on dislocations is, in contrast, relatively modest. At the same time, bubble sizes in the bulk and on extended defects fall down between the lowest and the highest ion implantation fluxes in a similar way, approximately twice. In contrast, the average size of bubbles on oxide particles decreases only slightly with the increase of flux, so that the ratio of the average sizes of bubbles on oxide particles and in the bulk increases, constituting approximately 1.9, 2.4, and 2.9 for the fluxes of 5×10^{11}, 1×10^{12}, and 5×10^{12} cm^{-2}s^{-1}, respectively. The bubbles on oxide particles are in one-to-one relation with Y_2O_3 precipitates and thus their number densities are insensitive to flux variations.

As can be concluded from the obtained data, the increase of the flux is accompanied with the decrease of the average bubble size and the increase of bubble number density for all families of bubbles. While the size decrease is in all cases quite moderate, the sensitivity of the bubble number density to flux variation depends on the bubble location. The number densities of the bubbles at grain boundaries and on dislocations demonstrate less than twofold increase, whereas the number density of the bubbles in the bulk increases by a factor of $\sim$ 8. As a result, the overall picture of the bubble distribution visibly changes upon transition from the lowest to the highest flux. While at the lowest flux the bubbles are preferentially located on structural defects (grain boundaries and dislocations), the bubbles in the bulk dominate at the highest one. One can also notice overall increase of the bubble number density.

Following the observed variations of the bubble microstructure, the increase of implantation flux from 5×10^{11} cm^{-2}s^{-1} to 5×10^{12} cm^{-2}s^{-1} resulted in the suppression of the overall swelling from $\sim$ 0.7 % down to $\sim$ 0.4%. The swelling caused by the grain boundary bubbles falls down most pronouncedly. The contribution from the bubble population on oxide particles remains practically unchanged at the level of 0.1%. In contrast, swelling from the bubbles in the bulk increases with the flux increase. As a result, while at the lowest flux the largest contribution to swelling is due to grain boundary bubbles, the strongest contributors at the highest flux become the bubbles in the bulk.

The difference in the swelling contribution variation with the implantation flux for different bubble populations reflects the competition between the trends for bubble size decrease and the number density increase. The notable increase of swelling contribution for bubbles in the

Table 5
Mean sizes and number densities of cavities associated with different microstructural features and their contributions to swelling, V/He ratio and the accumulated He fraction in ODS-EUROFER implanted with 10 keV He$^+$ ions to the fluence of 5×10^{15} cm^{-2} at $T = 823$ K with three different fluxes. Values marked with asterisks are estimates using equation (1).

5×10^{11} cm^{-2}s^{-1}	D_c^k (10^{-9} m)	N_V^k (10^{22} m^{-3})	S_k (%)	V/He$_k$	F_{He}^k (10^3appm)	F_{He}^k (%)
Grain boundaries	4.79 ± 0.35	5.32 ± 1.44	0.31 ± 0.09	1.83	1.69 ± 0.47	26.9 ± 7.6
Dislocations	4.69 ± 0.24	2.00 ± 0.23	0.11 ± 0.01	1.81	0.60 ± 0.07	9.6 ± 1.1
Carbide	3.55 ± 0.36	2.13 ± 0.21	0.05 ± 0.02	1.61	0.31 ± 0.10	5.0 ± 1.6
Y_2O_3	8.11 ± 0.81	1.00 ± 0.10	0.098 ± 0.031	2.35	0.42 ± 0.13	6.7 ± 2.1
Volume	4.36 ± 0.23	2.81 ± 0.46	0.12 ± 0.02	1.76	0.70 ± 0.12	11.2 ± 1.8
Total		13.26 ± 3.59	0.68 ± 0.22		3.72 ± 1.18	59.4 ± 18.8
1×10^{12} cm^{-2}s^{-1}	D_c^k (10^{-9} m)	N_V^k (10^{22} m^{-3})	S_k (%)	V/He$_k$	F_{He}^k (10^3appm)	F_{He}^k (%)
Grain boundaries	3.37 ± 0.28	7.43 ± 1.04	0.14 ± 0.03	1.58	0.95 ± 0.19	15.1 ± 3.1
Dislocations	3.32 ± 0.37	2.64 ± 0.36	0.051 ± 0.014	1.57	0.32 ± 0.09	5.2 ± 1.4
Carbide	2.66 ± 0.27*	2.13 ± 0.21*	0.021 ± 0.007*	1.44*	0.15 ± 0.05*	2.3 ± 0.7*
Y_2O_3	7.96 ± 0.80	1.00 ± 0.10	0.091 ± 0.029	2.33	0.40 ± 0.13	6.3 ± 2.0
Volume	3.28 ± 0.23	8.80 ± 2.61	0.16 ± 0.05	1.56	1.05 ± 0.33	16.7 ± 5.3
Total		22.0 ± 6.53	0.48 ± 0.15		2.86 ± 0.91	45.6 ± 14.5
5×10^{12} cm^{-2}s^{-1}	D_c^k (10^{-9} m)	N_V^k (10^{22} m^{-3})	S_k (%)	V/He$_k$	F_{He}^k (10^3appm)	F_{He}^k (%)
Grain boundaries	2.51 ± 0.18	8.91 ± 1.44	0.074 ± 0.016	1.42	0.53 ± 0.11	8.5 ± 1.8
Dislocations	2.51 ± 0.26	2.83 ± 0.40	0.023 ± 0.006	1.41	0.17 ± 0.05	2.6 ± 0.7
Carbide	2.04 ± 0.20*	2.13 ± 0.21*	0.010 ± 0.003*	1.32*	0.073 ± 0.023*	1.2 ± 0.4*
Y_2O_3	7.78 ± 0.78	1.00 ± 0.10	0.083 ± 0.026	2.30	0.36 ± 0.11	5.8 ± 1.8
Volume	2.65 ± 0.16	21.65 ± 9.35	0.21 ± 0.10	1.44	1.46 ± 0.65	23.3 ± 10.3
Total		36.52 ± 15.76	0.40 ± 0.18		2.59 ± 1.15	41.4 ± 18.3

bulk is mainly due to the sharp increase of their number density with the increase of the flux. Swelling contribution from bubbles attached to nanoparticles changes only slightly because their number density is independent of the flux, while the average size demonstrates only a minor reduction with increasing implantation flux (see Fig. 8(b)). For the other bubble families, the trend for size reduction dominates, resulting in the swelling contribution decrease.

The trends for the average V/He ratio variation follow those for bubble sizes. The largest value of V/He ~ 2.3 is estimated for the bubbles on oxide particles, which remain the largest whatever the flux. Bubbles associated with the other microstructural components and bubbles in the bulk demonstrate the decrease of V/He ratio (by a factor of 1.4) with the flux increase.

At the lowest flux used, the maximum share of helium is accumulated in the grain boundary bubbles. The increase of the flux significantly decreases the share of the implanted helium accumulated in the bubbles at grain boundaries and on dislocations and carbides. At the same time, the share of implanted He captured by bubbles in the bulk increases with the implantation flux, reaching ~ 23% at the highest flux. However, this increase does not compensate for the reduction in He inventory in the other bubble populations and the total estimated share of implanted helium accumulated in the bubbles visible in TEM decreases from ~ 59% at the lowest flux to ~ 41% at the highest one. The remaining helium atoms should be trapped in features undetectable by TEM.

Temperature variation effect on bubble parameters, contributions to swelling and helium inventory in different bubble families. The third set of experiments involved variation of ion implantation temperature while keeping fixed implantation flux and fluence. In this set of experiments, several samples were implanted at temperatures 723 K, 823 K, and 923 K with 10 keV He ions to the fluence of 5×10^{15} cm^{-2} using the flux of 5×10^{11} cm^{-2}s^{-1}.

In agreement with the other experiments, He bubbles extensively decorate grain boundaries, dislocations and precipitates (typical BF TEM images of ODS-EUROFER implanted at temperatures 723 K, 823 K, and 923 K are shown in Fig. S7 in the Supplementary materials). The sizes of bubbles on yttria nanoparticles are at all temperatures notably different from those on the other microstructural defects. Pronounced bubble size increase with the increasing temperature can be easily noticed.

The qualitative analysis of bubble array parameters starts as before with the determination of the average size of bubbles attached to oxide nanoparticles, as shown in Fig. 8(c). The effective average diameters of bubbles on oxide particles determined using the derived trend lines are found to be 8.0, 8.1, and 8.7 nm for the implantation temperatures 723 K, 823 K, and 923 K, respectively. In other words, $\langle D_c^p \rangle$ is not too sensitive to temperature variation in the studied range. At all studied temperatures one observes particles with bubbles larger than the particle itself (such bubbles are represented by points falling in the white area in Fig. 8(c)).

Table 6 summarizes the measured bubble parameters and estimated contributions to the swelling, V/H ratio and He inventory separately for each bubble family at temperatures 723, 823 and 923 K. Similar to the flux variation regime, the cited parameters for bubbles associated with carbides are evaluated for the upper and lower temperatures using the measured values for 823 K.

At each particular studied temperature, the average sizes of bubbles in the bulk, on dislocations and at the grain boundaries are quite similar, though the bubbles at the grain boundaries are typically slightly (by ~ 10%) larger than the others, whereas the bubbles associated with Y_2O_3 nanoparticles are visibly larger than on the other microstructural features.

The general trends for the bubble parameter variation with temperature are the same for the bubbles in the bulk and on extended defects. The mean bubble size increases with the increase of temperature. Correspondingly, since the average size of the bubbles on oxide particles weakly depends on temperature, the size difference between the bubbles associated with oxide particles and with the other microstructural features becomes less pronounced as the ion implantation temperature grows.

The total bubble volumetric number density decreases as the temperature increases from 723 to 923 K. The largest contribution to the total bubble number density at all studied temperatures comes from the bubbles at grain boundaries. The number density of the bubbles associated with dislocations is weakly sensitive to temperature. The most pronounced is the number density decrease for the bubbles in the bulk.

The estimated total swelling induced by all bubbles grows with the temperature in the studied temperature range, changing from ~ 0.5 % at 723 K to ~ 0.9% at 923 K. The same trend is demonstrated by all bubble populations, associated with microstructural defects. The main contribution to swelling comes from the bubbles at the grain boundaries. Only bubbles in the bulk demonstrate the inverse trend of slightly decreasing swelling contribution with the temperature increase. As a result, while at 723 K the swelling from the bubbles in the bulk is comparable to that from the bubbles at the grain boundaries, at 923 K it falls down to the level typical for other bubble populations.

The swelling increase for the bubbles on extended defects and oxide

Table 6
The contributions of bubbles associated with different microstructural features to bubble average size and number density, swelling, V/He ratio and the accumulated He fraction in ODS-EUROFER implanted with He$^+$ ions at different temperatures.

723 K	D_c^k (10^{-9} m)	N_V^k (10^{22} m^{-3})	S_k (%)	V/He$_k$	F_{He}^k (10^3 appm)	F_{He}^k (%)
Grain boundaries	3.62 ± 0.19	7.59 ± 1.19	0.19 ± 0.031	1.55	1.23 ± 0.20	19.6 ± 3.2
Dislocations	3.49 ± 0.26	2.48 ± 0.30	0.055 ± 0.009	1.53	0.37 ± 0.06	5.9 ± 1.0
Carbide	2.80 ± 0.28*	2.13 ± 0.21*	0.024 ± 0.008*	1.39*	0.17 ± 0.05*	2.7 ± 0.8*
Y₂O₃	8.01 ± 0.80	1.00 ± 0.10	0.093 ± 0.029	2.19	0.43 ± 0.14	6.9 ± 2.2
Volume	3.38 ± 0.39	5.99 ± 0.80	0.12 ± 0.03	1.51	0.81 ± 0.23	12.9 ± 3.6
Total		19.19 ± 3.01	0.48 ± 0.15		3.00 ± 0.95	48.0 ± 15.2
823 K	D_c^k (10^{-9} m)	N_V^k (10^{22} m^{-3})	S_k (%)	V/He$_k$	F_{He}^k (10^3 appm)	F_{He}^k (%)
Grain boundaries	4.79 ± 0.35	5.32 ± 1.44	0.31 ± 0.09	1.83	1.69 ± 0.47	26.9 ± 7.6
Dislocations	4.69 ± 0.24	2.00 ± 0.23	0.11 ± 0.01	1.81	0.60 ± 0.07	9.6 ± 1.1
Carbide	3.55 ± 0.36	2.13 ± 0.21	0.050 ± 0.016	1.61	0.31 ± 0.10	5.0 ± 1.6
Y₂O₃	8.11 ± 0.81	1.00 ± 0.10	0.098 ± 0.031	2.35	0.42 ± 0.13	6.7 ± 2.1
Volume	4.36 ± 0.23	2.81 ± 0.46	0.12 ± 0.02	1.76	0.70 ± 0.12	11.2 ± 1.8
Total		13.26 ± 3.59	0.68 ± 0.22		3.72 ± 1.18	59.4 ± 18.8
923 K	D_c^k (10^{-9} m)	N_V^k (10^{22} m^{-3})	S_k (%)	V/He$_k$	F_{He}^k (10^3 appm)	F_{He}^k (%)
Grain boundaries	5.40 ± 0.44	4.99 ± 0.59	0.41 ± 0.06	2.03	2.04 ± 0.29	32.5 ± 4.7
Dislocations	5.05 ± 0.42	1.98 ± 0.30	0.13 ± 0.02	1.97	0.69 ± 0.12	11.0 ± 2.0
Carbide	4.11 ± 0.41*	2.13 ± 0.21*	0.078 ± 0.025*	1.80*	0.44 ± 0.14*	7.0 ± 2.2*
Y₂O₃	8.73 ± 0.87	1.00 ± 0.10	0.14 ± 0.04	2.59	0.52 ± 0.17	8.4 ± 2.6
Volume	4.97 ± 0.52	1.96 ± 0.38	0.13 ± 0.03	1.96	0.64 ± 0.16	10.3 ± 2.6
Total		12.06 ± 2.34	0.883 ± 0.279		4.33 ± 1.37	69.2 ± 21.8

particles results from the noticeable growth of bubble average sizes. In contrast, for the bubbles in the bulk the growth of the average size is counterbalanced by the decreasing number density and thus the contribution of this bubble population to the swelling remains only weakly sensitive to the temperature variation.

The ratio V/He is the highest for the bubbles associated with nano-particles, which is quite natural having in mind that these bubbles are noticeably larger than those of all other bubble populations, whatever the temperature. However, for all other bubble families the ratio V/He also increases with the temperature due to the average bubble size growth.

Similar to the swelling, the increase of temperature from 723 to 923 K results in the notable increase (from ~ 48% to ~ 69%) for the esti-mated share of implanted He atoms that are accumulated in the visible bubbles. The largest part of He atoms is always captured in the grain boundary bubbles, which accommodate from ~ 20% of all He at 723 K to ~ 33% at 923 K. In contrast, the share of helium captured within the bubbles in the bulk somewhat decreases from ~ 13% down to ~ 10% when the implantation temperature grows from 723 K to 923 K.

Corrections to contributions to swelling and helium inventory due to the 'hidden' helium. The estimates of swelling in the previous sections were based on the conventional assumption that the increase of material volume is to a good accuracy equal to the volume of cavities produced by ion implantation, which can be directly evaluated from TEM measure-ments of cavity sizes and number densities. This assumption usually works well for purely void swelling not accompanied with helium accumulation in spite of the fact that TEM is able to resolve only cavities larger than a certain threshold size of, typically, ~1nm because in the common reactor operation conditions the relative share of free va-cancies and vacancies in small clusters is negligible as compared to the volume of visible voids. The situation changes when the radiation damage production by fast particles is accompanied with the efficient accumulation of helium, either created in transmutation reactions, or directly introduced by implantation (as is the case in this study). In many void swelling resistant metals, including ferritic-martensitic steels, the accumulation of helium under irradiation is accompanied with its pre-cipitation in small cavities filled with gas atoms. The early growth of gas-filled cavities (bubbles) is controlled by the number of gas atoms captured by the bubble. The bubble sizes are seldom very much larger than the TEM resolution threshold and there always exists a certain amount of gas atoms captured in small gas-vacancy clusters invisible in TEM. When the number of gas atom contained in the 'invisible' clusters is comparable to that accumulated in the visible bubbles, a straightfor-ward evaluation of the visible cavity volume can introduce a non-negligible underestimation of the true volume expansion of the material.

The estimates of helium fraction accumulated in the bubbles, as given in Tables 4-6, indicate that none of the applied implantation re-gimes provides close to 100% capture of the implanted helium by the whole visible bubble population and so a noticeable share of implanted He atoms should be located in small He-vacancy clusters invisible by TEM. In some studied helium implantation regimes, for instance at the highest flux of 5×10^{12} cm^{-2}s^{-1} or at the temperature of 723 K, the share of implanted helium trapped in all visible bubbles was estimated to be even less than 50% of the implanted amount. The swelling contribution from the small He-vacancy clusters was not reflected in the numbers given for the total swelling in Tables 4-6. In order to get a feeling for the level of the underestimation, the total swelling values that include contributions from both bubbles and small He-vacancy complexes were calculated for all implantation regimes used. In the calculations we tentatively assumed that He atoms captured in small He-vacancy clus-ters occupy on the average one vacancy. The resulting estimates are given in Table 7.

As can be concluded based on these estimates, the relative contri-bution of invisible clusters to the swelling changes only weakly with the

Table 7
Estimated cumulative values of V/He ratio, He fraction F_{He} in visible bubbles (in appm and as fractions of the total implanted He amount, F_{He_tot}), swelling esti-mated from TEM data (S_{TEM}) and total swelling that includes contribution from helium dissolved in small He-vacancy clusters.

| Fluence variation	<V/He>	F_{He} (10^3appm)	F_{He} (%)	S_{TEM} (%)	S_{total} (%)
1×10^{15} cm^{-2}, $F_{He\_tot} = 1.25 \times 10^3$appm	1.59	0.92 ± 0.29	73.1 ± 23.1	0.14 ± 0.05	0.18 ± 0.06
5×10^{15} cm^{-2}, $F_{He\_tot} = 6.3 \times 10^3$appm	1.87	3.72 ± 1.18	59.4 ± 18.8	0.68 ± 0.22	0.94 ± 0.30
1×10^{16} cm^{-2}, $F_{He\_tot} = 12.5 \times 10^3$appm	2.02	7.40 ± 2.34	59.0 ± 18.7	1.48 ± 0.48	2.00 ± 0.69
Flux variation					
5×10^{11} cm^{-2}s^{-1}, $F_{He\_tot} = 6.3 \times 10^3$appm	1.87	3.72 ± 1.18	59.4 ± 18.8	0.68 ± 0.22	0.94 ± 0.30
1×10^{12} cm^{-2}s^{-1}, $F_{He\_tot} = 6.3 \times 10^3$appm	1.70	2.86 ± 0.91	45.6 ± 14.5	0.47 ± 0.15	0.81 ± 0.26
5×10^{12} cm^{-2}s^{-1}, $F_{He\_tot} = 6.3 \times 10^3$appm	1.58	2.59 ± 1.15	41.4 ± 18.3	0.40 ± 0.18	0.77 ± 0.34
Temperature variation					
723 K, $F_{He\_tot} = 6.3 \times 10^3$appm	1.63	3.00 ± 0.95	48.0 ± 15.2	0.48 ± 0.15	0.81 ± 0.26
823 K, $F_{He\_tot} = 6.3 \times 10^3$appm	1.87	3.72 ± 1.187	59.4 ± 18.8	0.68 ± 0.22	0.94 ± 0.30
923 K, $F_{He\_tot} = 6.3 \times 10^3$appm	2.07	4.32 ± 1.37	69.2 ± 21.8	0.88 ± 0.28	1.08 ± 0.34

increasing fluence (remaining at the level of 20–25%) at the fixed im-plantation flux and temperature, but is quite sensitive to flux and tem-perature variations. In all considered cases, the swelling underestimation due to the neglect of helium dissolved in small vacancy clusters is non-negligible. As a general trend, one can expect that the application of the TEM image-based estimates of the bubble parameters can be rather inaccurate in experimental studies performed at low temperatures and using too high rates of He production/introduction in the matrix.

Microstructural evolution in ODS-EUROFER steel caused by RT implantation followed by post-implantation annealing

Helium pre-implantation at room temperature followed by post-implantation annealing (PIA) is a common way to simulate He accu-mulation in radiation materials science. However, it is not evident that this approach is suitable in the case of such complex material as ODS-EUROFER steel. That is, the bubble populations developed after a two-stage treatment is not necessarily representative of the bubble struc-tures developed directly during high-temperature He implantation. The goal of this section is to compare the general trends of microstructural evolution in ODS-EUROFER steel during high temperature He implan-tation with the results of an experiment performed using a combination of room temperature He pre-implantation and PIA (referred below as RT + PIA regime).

The post-implantation annealing of ODS-EUROFER samples implanted at RT with He ions up to the fluence of 5×10^{15} cm^{-2} was performed in vacuum (~10^{-5} Pa) for 90 min at 823 K. Typical BF TEM images of ODS-EUROFER samples after RT + PIA are shown in Fig. 9.

Qualitatively, observations for RT + PIA were in many respects similar to the relevant high-temperature implantation with the same flux and fluence (i.e. T = 823 K, flux 1×10^{12}cm^{-2}s^{-1}, fluence 5×10^{15} cm^{-2}). Helium bubbles were seen decorating different microstructural defects (grain boundaries, see Fig. 9(a), as well as dislocations and precipitates, see Fig. 9(b)), in addition to bubbles in the bulk. As can be seen in Fig. 9(a), the bubbles associated with grain boundaries look, on the average, slightly larger than those in the bulk and on dislocations.
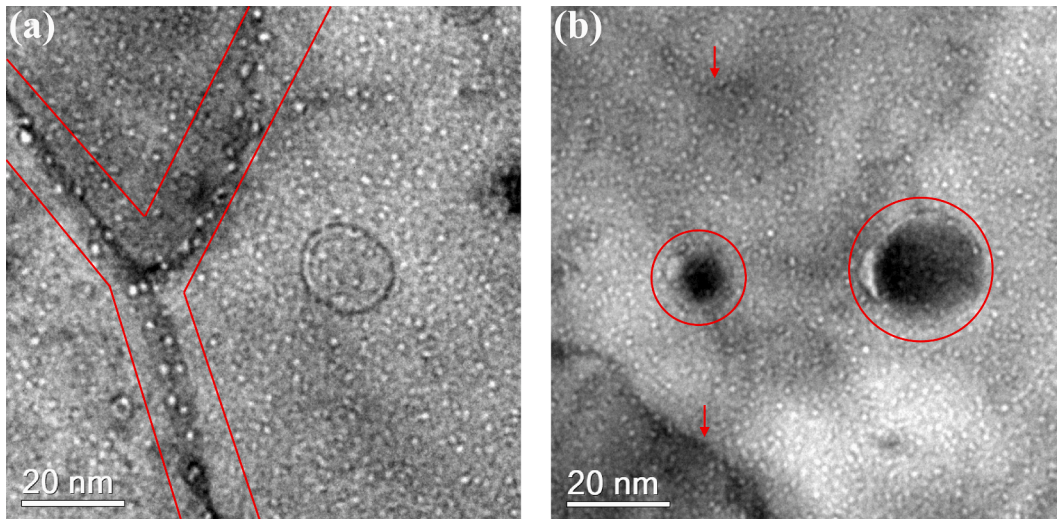
Fig. 9. Microstructure of ODS-EUROFER steel implanted with 10 keV He ions to the fluence of 5×10^{15} cm^{-2} at RT and subsequently annealed for 90 min at 823 K. BF TEM imaging conditions: ~ 0.8 μm underfocus.

Fig. 9(b) evidences that the bubbles attached to nano-oxides are noticeably larger than those belonging to all other bubble populations and the bubble sizes seem to correlate with the sizes of the host nano-oxide particles. But, in contrast to TEM images obtained after high temperature implantation, much higher density of tiny bubbles in the bulk can be immediately noticed in the RT + PIA sample.

In order to extract quantitative information from the TEM data, we use the same approach as that applied in the previous sections. We start with the bubbles associated with nano-oxides and determine their average size $\langle D_c^p \rangle$ from the measured dependence $D_c^p(D_p)$, as shown in Fig. 8(d).

As can be seen in Fig. 8(d), D_c^p increases from ~ 3 nm to ~ 10 nm as nanoparticle size increases from 5 to 23 nm, demonstrating the same qualitative trend as that observed after high temperature implantation. In comparison with the high temperature implantations, the bubbles on oxide particles are consistently smaller for the same particle size and no particles strongly enveloped by bubbles were found. Accordingly, the estimated average size for the bubbles on the oxide particles for the RT + PIA processing regime, $\langle D_c^p \rangle \approx 5.6$ nm, is smaller than that found for the high temperature implantation, $\langle D_c^p \rangle \approx 8$ nm.

Table 8 collects a summary of the calculated bubble parameters for different microstructural features in ODS-EUROFER steel sample after RT + PIA. The table contains no data for the bubbles on carbide particles because no $M_{23}C_6$ carbides were met in electron transparent zones of TEM samples implanted in this regime. However, according to the results of statistical analysis presented for the fluence variation case, carbides provide only minor contributions to the cumulative bubble number density, swelling and helium inventory. Therefore, the lack of the data for the bubbles attached to carbides is not expected to seriously affect the trends described below.

As can be noticed, the bubble population is dominated by the bubbles in the bulk, with the estimated number density $N_V^V \approx 1.9 \times 10^{24}$ m^{-3}. The

number density of the bubbles at grain boundaries is more than an order magnitude lower than in the bulk, while the number densities of the bubbles on dislocations and oxide particles are even less.

As a result of their very high number density, the bubbles in the bulk provide the main contributions to the overall swelling, $\langle S_V \rangle \approx 0.44$ %, and the fraction of accumulated helium, $\langle F_{He}^p \rangle \approx 58$%, even though these bubbles have smaller average size than the bubbles associated with extended defects and particles. The contributions to the swelling and the helium inventory from all other bubble populations are relatively minor.

A comparison of the bubble parameters between the RT + PIA and high temperature implantation regimes is shown in Fig. 10 separately for each bubble population.

Despite very similar values of cumulative swelling for the RT + PIA and high temperature implantation regimes (excluding the impact of carbides), the parameters of bubbles at different microstructural components and the contributions of different bubble populations to swelling and helium inventory differ considerably. In general, the bubbles formed after RT + PIA are smaller than the bubbles formed after the high temperature implantation by roughly a factor of 2 (see Fig. 10(a)). Only for the bubbles attached to nano-oxide particles the difference in sizes is found to be relatively small. The bubble number densities show the opposite trend (see Fig. 10(b)); those after RT + PIA are always higher than after the implantation at the high temperature. The enormous number density increase for the bubbles in the bulk results in a significant re-distribution of bubble population impacts on the swelling and helium inventory. While in the high-temperature implantation regime the bubbles at the grain boundaries and in the bulk contribute to the swelling and the accumulated helium fraction in similar shares, the swelling and helium inventory after RT + PIA are both dominated by the bubbles in the bulk. Finally, it can be noticed that RT + PIA promotes overall more efficient He clustering in the visible bubbles, which collect ~ 71% of all implanted He, while for the high temperature implantation the share of He collected in the visible bubbles is only ~ 43%.

Table 8
The contributions of bubbles associated with different microstructural features to bubble average size and number density, swelling, V/He ratio and the accumulated He fraction in ODS-EUROFER processed in RT + PIA regime.

|	D_c^k (10^{-9} m)	N_V^k (10^{22} m^{-3})	S^k (%)	V/He	F_{He}^k (10^{3}appm)	F_{He}^k(%)
Grain boundaries	2.10 ± 0.18	15.39 ± 2.54	0.075 ± 0.02	1.33	0.57 ± 0.15	9.0 ± 2.3
Dislocations	1.72 ± 0.10	4.83 ± 0.82	0.013 ± 0.003	1.24	0.10 ± 0.02	1.7 ± 0.3
Y$_2$O$_3$	5.62 ± 0.56	1.00 ± 0.01	0.021 ± 0.01	1.97	0.11 ± 0.03	1.7 ± 0.5
Volume	1.65 ± 0.11	189.02 ± 28.38	0.44 ± 0.10	1.23	3.65 ± 0.79	58.2 ± 12.6
Total		210.24 ± 35.50	0.55 ± 0.18		4425 ± 1399	70.6 ± 22.3
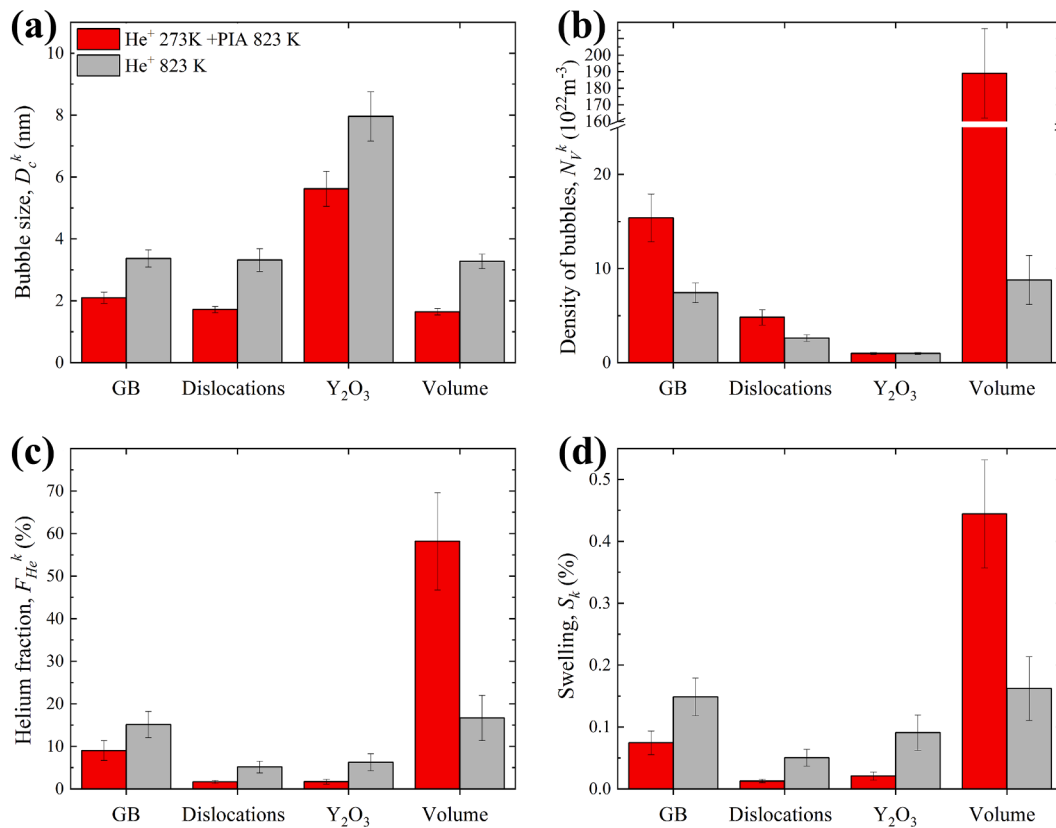
Fig. 10. Comparative statistical analysis of bubble mean size, volume density of bubbles, swelling and He fraction contributions for the bubbles associated with different microstructural components in ODS-EUROFER implanted by He$^+$ ions either in RT + PIA regime (red bars), or directly at 823 K (grey bars). Color references in panel (a) are applicable for all panels. Data for high-temperature regime are adopted from Table 5. (For interpretation of the references to color in this figure legend, the reader is referred to the web version of this article.)

Helium partitioning between bubbles at different microstructural defects and cumulative swelling in EUROFER 97 in comparison to ODS-EUROFER

In order to better understand the relative role of yttria nanoparticles in the helium accumulation kinetics in ODS-EUROFER steel, it is instructive to compare the general trends of the ODS-EUROFER microstructural evolution under helium implantation with those in the oxide particle free material with a similar composition, that is EUROFER 97 steel. This section summarizes the results of TEM investigations of EUROFER 97 steel implanted with helium in the experimental setup similar to that used for ODS-EUROFER. As shown in section 3.1, the elemental content and phase composition of ODS-EUROFER and EUROFER 97 are similar. The main difference is in the grain structure, which is more complicated in EUROFER 97 in the tempered condition. To the best of our knowledge, there is no detailed database quantitatively characterizing the microstructure of EUROFER 97 steel, including e.g. the relative densities of grain boundaries of various kinds (prior austenite / packet / block / lath), or carbide precipitates ($M_{23}C_6$ and MX). The lack of such data precludes the estimation of helium partitioning between different microstructural features and the estimation of their contribution to swelling in EUROFER 97. So here we restrict us to the direct comparison of bubble sizes and specific number densities (see Ref. [25]) on different types of microstructural features in EUROFER 97 and ODS-EUROFER, while for the comparison of swelling and the fraction of helium accumulated in the bubbles only cumulative value estimates will be used.

The typical microstructure of EUROFER 97 implanted with He ions to the fluence of 1×10^{16} cm^{-2} at 823 K is shown in Fig. 11. Many bubbles are associated with various microstructural features. As a result, the bubbles are non-uniformly spatially distributed following local variations in associated microstructure. Cubic He bubbles decorate grain
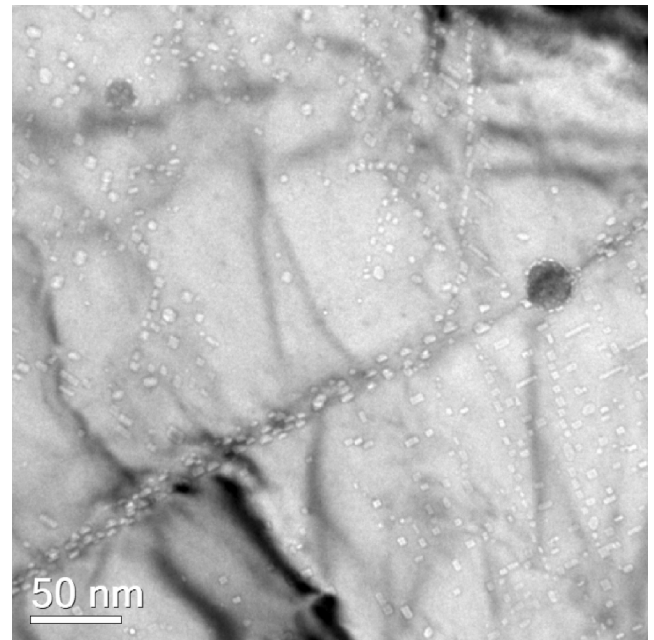
Fig. 11. Typical microstructure of EUROFER 97 implanted with He ions to 1 × 10^{16} cm^{-2} at 823 K. BF TEM imaging conditions: (a) ~ 1 μm underfocus.

boundaries, dislocations, and second phase precipitates and appear to be similar in size to the bubbles in the grain interior.

Fig. 12 shows regions containing grain boundary $M_{23}C_6$ carbides
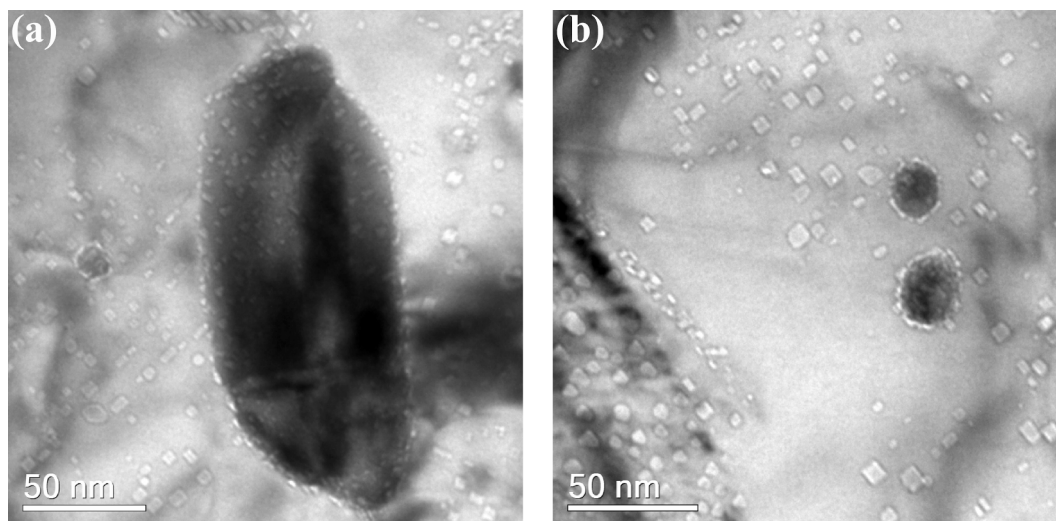
Fig. 12. Carbide precipitates in EUROFER 97 implanted at 823 K with He ions to the fluence of 1×10^{16} cm^{-2}: (a) MC carbide, (b) $M_{23}C_6$ carbide. BF TEM imaging conditions: ~ 0.5 μm underfocus.

(Fig. 12(a)) and intragranular carbonitride MX precipitates (Fig. 12(b)) characteristic for EUROFER 97 steel. Both types of precipitates are heavily decorated with large numbers of relatively small bubbles. The sizes of bubbles attached to both types of carbides look similar.
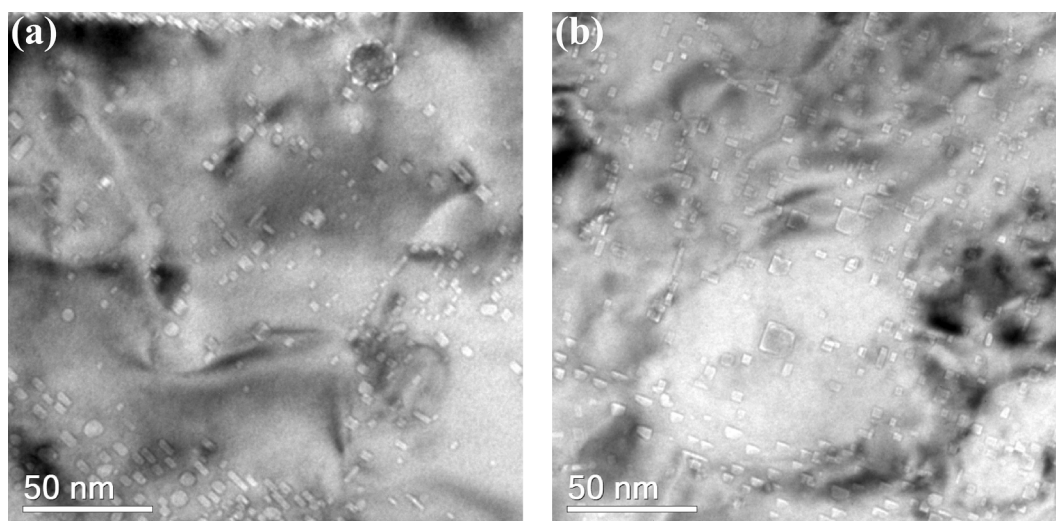
Typical TEM images of EUROFER 97 and ODS-EUROFER samples implanted under the same conditions are compared in Fig. 13. Judging from Figs. 11-13, the general trends of the microstructure development in ODS-EUROFER and its non-ODS counterpart look qualitatively very similar, i.e. helium bubbles with similar sizes are distributed between structural defects. In order to obtain a basis for more detailed comparison, the parameters of bubble ensembles related to each microstructural defect type in both materials were estimated quantitatively, as described below.

As demonstrated in section 3.2.2, helium in ODS-EUROFER steel shows notably different behavior at the yttria/matrix and carbide/matrix interfaces. Typically, the surface of carbides is covered by multiple small bubbles, while the oxide precipitates host single (very rarely a couple of) relatively large bubbles. However, a straightforward comparison of these precipitate types in ODS-EUROFER steel was not quite fair because of very different size of $M_{23}C_6$ carbides (~100 nm) and Y_2O_3 (~12 nm) oxide precipitates. In contrast, in EUROFER 97 steel

various types of carbonitride MX precipitates (including (Ta,V)C, TaC and VN) with the mean size (~20 nm) comparable to that of yttria nanoparticles in ODS-EUROFER are present. Having in mind similar sizes of carbonitride precipitates in EUROFER 97 and oxide particles in ODS-EUROFER, it is instructive to compare helium trapping on such precipitates under the same implantation conditions. Fig. 14(a) and (b) show BF TEM micrographs of a MX precipitate in EUROFER 97 and an Y_2O_3 precipitate in ODS-EUROFER, respectively, after He implantation in identical conditions. As can be seen in Fig. 14(a), the MX precipitate (~15 nm in diameter) in EUROFER 97 steel is decorated with multiple relatively small He bubbles (slightly smaller than those in the surrounding matrix), similar to large $M_{23}C_6$ carbides in both materials. In contrast, under the same implantation conditions helium is collected at the Y_2O_3 nanoparticle/matrix interface in a single bubble with notably larger size than the typical size of bubbles in the matrix (Fig. 14(b)).

The results of comparative statistical analysis of specific number densities (per defect) and average sizes of helium bubbles associated with different microstructural features in EUROFER 97 and ODS-EUROFER steels are summarized in Table 9 and Fig. 15.

Bubbles in EUROFER 97 steel are slightly larger than in ODS-EUROFER, no matter whether they are located in the bulk or on

Fig. 13. Microstructure of EUROFER 97 (a) and ODS-EUROFER (b) implanted at 823 K with He ions to the fluence of 1×10^{16} cm^{-2}. BF TEM imaging condition ~ 0.8 μm underfocus.
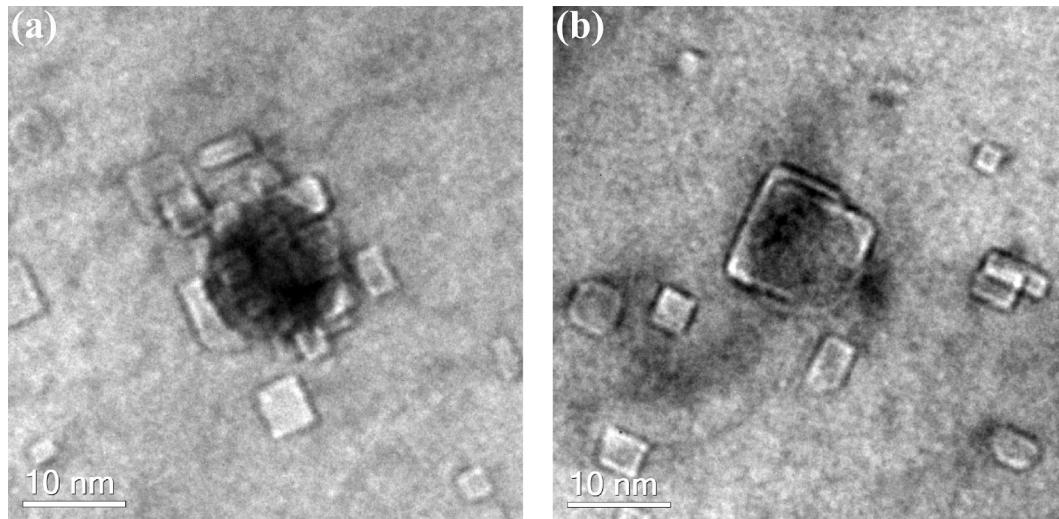
Fig. 14. MX precipitate in EUROFER 97 (a) and yttria precipitate in ODS-EUROFER (b) steels implanted with He ions to the fluence of 1×10^{16} cm^{-2}at 823 K. BF TEM imaging conditions: ~ 0.5 µm underfocus.

Table 9
Comparative statistical analysis of specific number densities N and sizes D of He bubbles associated with different microstructural features in EUROFER 97 and ODS-EUROFER steels. Data for ODS-EUROFER are borrowed from Table 5.

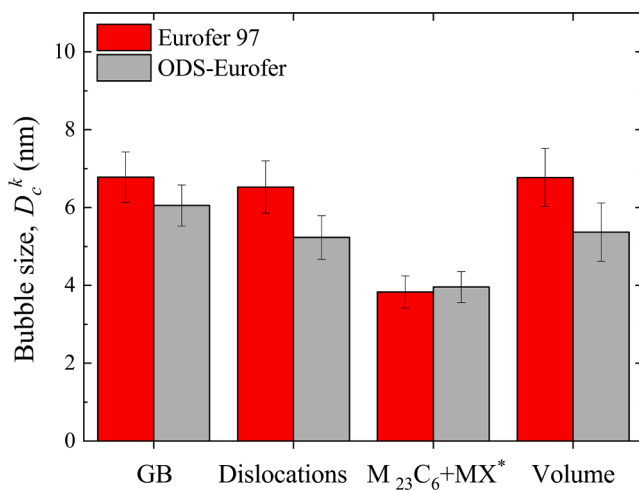|	Volume		Grain boundaries		Dislocations		Carbides	
	N, 10^{22}m^{-3}	D, nm	N, 10^{15} m^{-2}	D, nm	N, 10^8 m^{-1}	D, nm	N, 10^{16} m^{-2}	D, nm
EUROFER97	7.32 ± 1.72	6.77 ± 0.75	7.87 ± 1.08	6.78 ± 0.65	1.54 ± 0.16	6.53 ± 0.67	3.35 ± 0.59	3.83 ± 0.41
ODS-EUROFER	5.40 ± 1.24	5.37 ± 0.75	7.07 ± 0.76	6.05 ± 0.53	1.54 ± 0.16	5.23 ± 0.56	2.40 ± 0.24	3.96 ± 0.40

Fig. 15. The average sizes of He bubbles associated with different microstructural defects in EUROFER 97 and ODS-EUROFER implanted to the fluence of 1×10^{16}cm^{-2} at T = 823 K with a flux 5×10^{11} cm^{-2}s^{-1}. * MX precipitates are observed only in EUROFER 97.

microstructural defects, except carbide precipitates. The average sizes of bubbles at carbides are the same in both materials. A similar trend is found for the density of helium bubbles (per defect). In general, all the calculated number densities are higher in EUROFER 97, excluding the bubbles on dislocations, whose specific number densities (per unit length of dislocation) are practically the same.

A detailed comparison of expected swelling and helium fraction captured in the bubbles belonging to different populations is currently impossible due to the lack of the necessary microstructural data for EUROFER 97. Hence, two simplified approaches were used to roughly estimate the expected swelling in EUROFER 97, namely – the standard ASTM approach, which uses the average bubble size and number density regardless of bubble association with that or other microstructural defects, and an indirect approach (these swelling estimates will be referred to below as S_{ASTM} and $S_{indirect}$, respectively). In the latter approach, the swelling is estimated as,

$$S_{indirect}(\%) = \langle V_c \rangle \bullet \sum_k N_V^k \bullet 100\%$$

where $\langle V_c \rangle$ is the volume of a single bubble averaged over all microstructural defect types in five different investigated areas and additionally averaged over investigated areas, while $\sum N_v$ is the total bubble number density in all studied areas. Helium fraction $\langle F_{He} \rangle$ was calculated in the same way as for ODS-EUROFER from the visible bubble volumes, taking into account the volume density of all visible helium bubbles $\sum N_v$ and the average bubble volume $\langle V_c \rangle$.

The calculated values of swelling, V/He ratio and helium fraction are collected in Table 10.

As might be expected from the larger sizes and densities of helium bubbles in EUROFER 97, higher values of swelling and accumulated helium fraction for EUROFER 97 in comparison to ODS-EUROFER are predicted. The increase in swelling is expected to constitute 50 to 60%, depending on the approach (standard or indirect) used for swelling estimation in EUROFER 97. The average V/He ratio in the bubbles is practically the same for both steels. Around 90% of implanted helium in EUROFER 97 is estimated to be captured in the visible bubbles in contrast to ODS-EUROFER, where the captured fraction is only around 60% of the total implanted He amount. The higher values of the accumulated helium fraction and swelling for EUROFER 97 steel in comparison with ODS-EUROFER could be associated with both the larger grain size of EUROFER 97 and the absence of Y$_2$O$_3$ nanoparticles.

Table 10

Cumulative values of helium bubble number density, V/He ratio, swelling estimated from TEM data, and He fraction for EUROFER 97 and ODS-EUROFER steels at the He fluence of 1×10^{16} cm^{-2} ($F_{He\_tot} = 1.25 \times 10^4$ appm).

	N_V, 10^{23} m^{-3}	$S_{indirect}$, %	S_{ASTM}, %	<V/He>	F_{He} (10^3 appm)	F_{He} (%)
EUROFER 97	1.93 ± 0.21	2.22 ± 0.44	2.35 ± 0.40	2.03	11019 ± 2174	87.9 ± 17.3
ODS-EUROFER	1.61 ± 0.37	1.48 ± 0.48	–	2.02	7401 ± 2340	59.0 ± 18.7

Discussion

The main objective of this study is the clarification of the relative importance of Y_2O_3 nanoparticles as helium trapping sites in ODS-EUROFER and estimation of potential risks associated with oxide nanoparticles in conditions of ODS steel operation in a high He/dpa ratio environment. Having this in mind, let us discuss the results of ODS-EUROFER steel characterization after single-beam He$^+$ implantations.

First of all, the estimates of the helium fraction accumulated in bubbles based on TEM observations indicate that in neither of studied implantation regimes the implanted helium is fully trapped in the visible bubbles. A noticeable share of implanted He atoms remains captured in traps invisible by TEM. Helium partitioning between the bubbles and the small He-V clusters is found to be sensitive to fluence, flux and temperature variations. A graphic summary of the observed trends can be found in Fig. S8 in the Supplementary materials. Depending on particular implantation conditions, the potential contribution of invisible He traps can constitute up to ~ 50% of the total swelling, indicating that the estimates of swelling and captured He fraction based on the summary volume of visible bubbles in TEM images can be quite inaccurate in experimental studies performed at low temperatures, high He concentrations and high rates of He production/introduction.

A remarkable feature of the observed bubble growth kinetics in all studied implantation regimes is the formation of different bubble families that grow not only in the grain bulk but also on microstructural defects, such as extended defects (dislocations, grain boundaries) and second-phase particles (carbides and oxides). The kinetics of the bubbles on oxide particles is notably different from that for all other bubble populations, where the bubble sizes and number densities depend strongly on the implantation conditions. In contrast, the number density of bubbles on Y_2O_3 nanoparticles is predetermined by the number density of oxide particles that typically host a single He bubble per particle and is thus not affected by the implantation conditions. Bubbles on oxide particles are pronouncedly larger than bubbles of other populations and the sizes of bubbles associated with yttria nanoparticles are less sensitive to variations of implantation conditions in the studied parameter ranges than to the sizes of host nanoparticles.

Restricting us below to the helium fraction and swelling associated with the bubbles, let's discuss briefly the relative contributions of the different bubble populations to these values in different He implantation regimes (a helpful graphic representation of the observed trends can be found in Figs. S9 and S10 in the Supplementary materials).

In the majority of studied implantation regimes both swelling and He inventory are largely controlled by bubble populations on structural defects (particles, dislocations and grain boundaries), while bubbles in the grain bulk provide relatively minor contribution. In quantitative terms, the relative contributions to helium accumulation and consequently swelling from bubbles on structural defects and in the grain bulk are mostly sensitive to variations of the implantation flux. As the implantation flux increases, the relative role of the bubbles in the bulk becomes stronger and at the highest flux of ~ 6 appm He/s this bubble population provides roughly the same contribution to swelling and helium inventory as bubbles on structural defects. With the increase of implantation fluence (helium concentration) and the decrease of temperature the relative contribution of bubbles in the grain bulk also increases, but for fluence and temperature variations within the studied ranges remains well below that from the bubbles on structural defects.

Among the bubble populations associated with structural defects, the most important contributors to both swelling and He inventory are the bubbles located at grain boundaries. Only bubbles in the grain bulk can serve as serious competitors in certain cases, mainly at high He fluxes and, to less extent, at high helium fluences. The strong contribution of grain boundaries to the helium inventory and swelling in the He implantation regimes used in this study results mainly from the small grain size of ODS-EUROFER and consequently high density of grain boundaries and the associated bubbles. The average size of bubbles at grain boundaries is typically larger than for the bubbles in the grain bulk, on dislocations or carbide precipitates, but only moderately. Even at the highest achieved He content of ~ 12000 appm we have observed no grain boundary bubble coalescence that might lead to the formation of huge bubbles and promote high-temperature helium embrittlement.

In spite of being pronouncedly larger than bubbles of all other populations in all He implantation regimes used, the bubbles on oxide particles contribute to helium accumulation and swelling by only less than 15% and 21%, respectively. The relatively minor role of Y_2O_3 nanoparticles in the helium inventory and swelling is primarily due to the low number density of nanoparticles in ODS-EUROFER steel, which coincides with that of oxide particles. It is worth mentioning, however, that the contributions of bubbles on oxide particles to both swelling and He inventory, even though remaining well below those from grain boundary bubbles, are comparable to those from all other bubble families in most implantation regimes, with the only exception of the high flux regime, where they considerably concede also to the bubbles in the grain bulk.

Finally, it should be emphasized that the helium implantation regimes used in this study are very different from the conditions expected in fusion or spallation reactor environments, where gas accumulation rates are expected to be few orders of magnitude lower, while the damage rate - notably higher than in our experiments [13]. Therefore, quantitative estimates of swelling and helium partitioning between the different bubble families obtained for ODS-EUROFER steel in this study are not directly relevant for fusion or spallation facilities. However, the qualitative trends in helium partitioning between the bubble families and their swelling contributions in ODS-EUROFER steel can be extrapolated on the reactor in-service conditions. In particular, the bubbles associated with Y_2O_3 nanoparticles in ODS-EUROFER steel, similar to bubbles on dislocations and carbides, are expected to provide only a minor contribution to both He inventory and swelling in the reactor operation conditions, unless they launch bubble-to-void transition (which, unfortunately, cannot be excluded for low He/dpa ratios [25]). Due to quite low grain size in ODS-EUROFER steel and high temperatures expected in fusion and spallation reactors, the main contribution to both swelling and helium inventory will most probably come from grain-boundary bubbles. Even though the bubbles in the grain bulk were found in this study to be competitive with the grain-boundary bubbles in certain regimes (high helium flux of fluence), these regimes (especially high flux that promotes dense bubble arrays in the bulk) are not relevant for the expected reactor operation conditions.

Conclusions

The observed trends in bubble growth kinetics, swelling and helium redistribution in ODS-EUROFER steel implanted with He ions to relatively high helium contents (thousands of appm) in reply to the variation of implantation parameters can be summarized as follows.

1. In all studied ion implantation regimes the formation of He bubbles was observed both in the bulk and on various structural defects, including grain boundaries, dislocations, carbide precipitates and yttria oxide particles. The estimates of the He inventory in the bubbles visible in TEM indicate that a noticeable share of He (20 to 50 % depending on the particular combination of implantation parameters) is trapped also in vacancy-helium clusters invisible by TEM.

2. Regardless of the ion implantation conditions applied, all Y_2O_3 nanoparticles were decorated with single (very rarely – two) He bubbles and the sizes of these bubbles were visibly larger than for the bubbles in the bulk and on extended defects. The sizes of bubbles attached to yttria nanoparticles correlated with the sizes of host particles, demonstrating a trend for the larger particles to host larger bubbles; this trend holds for all ion implantation conditions used. But in spite of relatively large bubble size, the estimated contributions from the bubbles associated with oxide particles to the He inventory and swelling were minor in all investigated regimes due to the moderate number density of Y_2O_3 particles in ODS-EUROFER steel. Thus, our results do not support the opinion that the helium trapping in bubbles on oxide nanoparticles can efficiently prevent helium accumulation on grain boundaries. However, the formation of bubbles on grain boundaries, even though not strongly affected by the presence of oxide nanoparticles even at the highest fluence (12000 appm) and temperature (923 K), did not led to bubble coalescence, which might be dangerous in terms of promoting the high-temperature intergranular embrittlement.

3. The increase of the implantation fluence from 10^{15} cm^{-2} to 10^{16} cm^{-2} at the fixed ion flux of 5×10^{11} cm^{-2}s^{-1} and irradiation temperature 823 K demonstrated the following trends in the helium bubble microstructure development, swelling and He inventory:

- the most important contributor to both swelling and He inventory was the population of the bubbles on grain boundaries.
- the helium capture efficiency in the bubbles on extended defects and second phase precipitates tended to saturate with fluence, but the bubbles in the bulk continued growing, becoming with the increase of dose competitive with the grain boundary bubble population as traps for helium introduced by ion implantation.

4. The increase of the implantation flux from 5×10^{11} cm^{-2}s^{-1} to 5×10^{11} cm^{-2}s^{-1} resulted in:

- the increase of number density and the decrease of the average size of all bubble populations, both in the bulk and on structural defects. As a result, the total swelling and the relative share of implanted helium accumulated in the bubbles decreased as the flux grew.
- the transition from preferential He accumulation in bubbles associated with structural defects to bubbles in the bulk. While at the lowest used flux of 5×10^{11} cm^{-2}s^{-1} the largest contribution to swelling and the largest share of accumulated helium are due to the bubbles at the grain boundaries, at the highest flux of 5×10^{12} cm^{-2}s^{-1} both the swelling and helium accumulation are largely controlled by the bubbles in the bulk.
- the increase of the share of implanted He captured in invisible sinks from $\sim$ 40% to $\sim$ 60%.

5. The variation of the sample temperature during ion implantation from 723 to 923 K resulted in the growth of the bubble average size and simultaneous decrease of the bubble number densities for all bubble families (with the only exception of oxide-associated bubble population, whose number density remained constant and equal to the number density of oxide particles). Both the swelling and helium inventory in the bubbles associated with microstructural defects noticeably grew in reply to the implantation temperature increase. For all temperatures, the grain boundary bubbles gave the largest contributions to both swelling and helium inventory, which grew with the increase of temperature. A similar trend was observed for the bubbles on the other extended defects and on the nanoparticles, though their individual contributions were remarkably lower than those from the grain boundary bubbles. In contrast, the bubbles in the bulk manifested relatively weak temperature sensitivity of contributions to both the swelling and helium inventory; both contributions decreased with the temperature increase, contrary to the overall trend.

6. A combination of room temperature ion implantation with subsequent annealing at 823 K was found to rather poorly reproduce the microstructural development in ODS-EUROFER steel observed during high temperature implantation with similar parameters. Even though the cumulative swelling in both implantation regimes was similar, the roles of bubble populations in the bulk and on structural defects differed significantly. Only the nano-oxides demonstrated very similar potential for helium storage during both implantation regimes. The significant difference between the He bubble populations after low and high temperature implantations indicates that the resulting gas-driven microstructure is primarily determined by the helium re-distribution at the implantation stage and is not much affected by helium mobility at the annealing stage.

7. Comparison of the results of He implantation into ODS-EUROFER and its oxide-free counterpart EUROFER 97 has demonstrated that, in spite of similar qualitative trends in the bubble population development, the bubbles in EUROFER 97 are larger and seem to trap the absolute majority of implanted He atoms in visible bubbles. As a result, the swelling estimated based on the volume of bubbles visible in TEM is also $\sim$ 50% larger than in ODS-EUROFER in practically the same implantation conditions. Higher values of accumulated helium fraction and swelling for EUROFER 97 steel in comparison to ODS-EUROFER could be associated with both the larger grain size of EUROFER 97 and the absence of Y_2O_3 nanoparticles.

8. Even at the highest achieved He content of 12,000 appm, the swelling estimated from the whole visible bubble population did not exceed 1.5 % and no indication of bubble-to-void transition was found. This evidences high resistance of ODS-EUROFER steel to swelling during helium accumulation to very high doses.

CRediT authorship contribution statement

Declaration of Competing Interest

The authors declare the following financial interests/personal relationships which may be considered as potential competing interests: [O. Emelyanova reports financial support was provided by French Embassy in Moscow. A. Gentils reports a relationship with French Federation for Fusion FR-FCM that includes: funding grants.].

Data availability

Data will be made available on request.

Acknowledgements

Appendix A. Supplementary material

Supplementary data to this article can be found online at https://doi.org/10.1016/j.nme.2023.101456.

References

[1] P. Yvon, Structural materials for generation IV nuclear reactors, Woodhead Publishing (2017), https://doi.org/10.1016/C2014-0-03589-7.

[2] G.R. Odette, S. Zinkle, Structural alloys for nuclear energy applications, Elsevier (2019), https://doi.org/10.1016/C2011-0-07772-4.

[3] I.L. Pioro, Handbook of generation IV nuclear reactors, Woodhead Publishing (2016), https://doi.org/10.1016/C2014-0-01699-1.

[4] S.J. Zinkle, J.T. Busby, Structural materials for fission & fusion energy, Mater. Today 12 (11) (2009) 12–19, https://doi.org/10.1016/S1369-7021(09)70294-9.

[5] S.J. Zinkle, G.S. Was, Materials challenges in nuclear energy, Acta Mater 61 (3) (2013) 735–758, https://doi.org/10.1016/j.actamat.2012.11.004.

[6] Structural Materials for Liquid Metal Cooled Fast Reactor Fuel Assemblies-Operational Behaviour (NF-T-4.3. INTERNATIONAL ATOMIC ENERGY AGENCY, 2012. [Online]. Available: https://www.iaea.org/publications/8872/structural-materials-for-liquid-metal-cooled-fast-reactor-fuel-assemblies-operational-behaviour.

[7] R. Lindau, A. Möslang, M. Rieth, M. Klimiankou, E. Materna-Morris, A. Alamo, A.-A.-F. Tavassoli, C. Cayron, A.-M. Lancha, P. Fernandez, N. Baluc, R. Schäublin, E. Diegele, G. Filacchioni, J.W. Rensman, B.v.d. Schaaf, E. Lucon, W. Dietz, Present development status of EUROFER and ODS-EUROFER for application in blanket concepts, Fusion Eng. Design 75–79 (SUPPL) (2005) 989–996, https://doi.org/10.1016/j.fusengdes.2005.06.186.

[8] S. Ukai, S. Ohtsuka, T. Kaito, Y. de Carlan, J. Ribis, J. Malaplate, 10 - Oxide dispersion-strengthened/ferrite-martensite steels as core materials for Generation IV nuclear reactors, structural materials for generation IV nuclear reactors, Woodhead Publishing, 2017, pp. 357–414.

[9] S.J. Zinkle, J.L. Boutard, D.T. Hoelzer, A. Kimura, R. Lindau, G.R. Odette, M. Rieth, L. Tan, H. Tanigawa, Development of next generation tempered and ODS reduced activation ferritic/martensitic steels for fusion energy applications, Nucl. Fusion 57 (2017) 92005, https://doi.org/10.1088/1741-4326/57/9/092005.

[10] G.R. Odette, D.T. Hoelzer, Irradiation-tolerant nanostructured ferritic alloys: transforming helium from a liability to an asset, JOM 62 (2010) 84–92, https://doi.org/10.1007/s11837-010-0144-1.

[11] G.R. Odette, M.J. Alinger, B.D. Wirth, Recent developments in irradiation-resistant steels, Annu. Rev. Mater. Res. 38 (2008) 471–503, https://doi.org/10.1146/annurev.matsci.38.060407.130315.

[12] G.R. Odette, N.J. Cunningham, T. Stan, M.E. Alam, and Y. de Carlan, Chapter 12 - Nano-Oxide Dispersion-Strengthened Steels, Structural Alloys for Nuclear Energy Applications. Elsevier, 2019, pp.529-583. doi: Doi: 10.1016/B978-0-12-397046-6.00012-5.

[13] P. Vladimirov, A. Möslang, Comparison of material irradiation conditions for fusion, spallation, stripping and fission neutron sources, J. Nucl. Mater. Part A 329–333 (2004) 233–237, https://doi.org/10.1016/j.jnucmat.2004.04.030.

[14] P.D. Edmondson, C.M. Parish, Y. Zhang, A. Hallén, M.K. Miller, Helium bubble distributions in a nanostructured ferritic alloy, J. Nucl. Mater. 434 (2013) 210–216, https://doi.org/10.1016/j.jnucmat.2012.11.049.

[15] A.I. Ryazanov, O.K. Chugunov, S.M. Ivanov, S.T. Latushkin, R. Lindau, A. Möslang, A.A. Nikitina, K.E. Prikhodko, E.V. Semenov, V.N. Unezhev, P.V. Vladimirov, Tensile properties and microstructure of helium implanted EUROFER-ODS, J. Nucl. Mater. 442 (SUPPL. 1) (2013) S153–S157, https://doi.org/10.1016/j.jnucmat.2013.03.080.

[16] T. Chen, H. Kim, J.G. Gigax, D. Chen, C.-C. Wei, F.A. Garner, L. Shao, Radiation response of oxide-dispersion-strengthened alloy MA956 after self-ion irradiation, Nucl. Instrum. Methods Phys. Res. B 409 (2017) 259–263, https://doi.org/10.1016/j.nimb.2017.05.024.

[17] Q. Li, C.M. Parish, K.A. Powers, M.K. Miller, Helium solubility and bubble formation in a nanostructured ferritic alloy, J. Nucl. Mater. 445 (2014) 165–174, https://doi.org/10.1016/j.jnucmat.2013.10.048.

[18] C.M. Parish, M.K. Miller, Aberration-corrected X-ray spectrum imaging and fresnel contrast to differentiate nanoclusters and cavities in helium-irradiated alloy 14YWT, Microscopy and Microanalysis 20 (2014) 613–626, https://doi.org/10.1017/S1431927614000312.

[19] C.M. Parish, K.A. Unocic, L. Tan, S.J. Zinkle, S. Kondo, L.L. Snead, D.T. Hoelzer, Y. Katoh, Helium sequestration at nanoparticle-matrix interfaces in helium + heavy ion irradiated nanostructured ferritic alloys, J. Nucl. Mater. 483 (2017) 21–34, https://doi.org/10.1016/j.jnucmat.2016.10.038.

[20] T. Yamamoto, G.R. Odette, P. Miao, D.J. Edwards, R.J. Kurtz, Helium effects on microstructural evolution in tempered martensitic steels: In situ helium implanter studies in HFIR, J. Nucl. Mater. 386–388 (2009) 338–341, https://doi.org/10.1016/j.jnucmat.2008.12.134.

[21] G.R. Odette, P. Miao, D.J. Edwards, T. Yamamoto, R.J. Kurtz, H. Tanigawa, Helium transport, fate and management in nanostructured ferritic alloys: In situ helium implanter studies, J. Nucl. Mater. 417 (2011) 1001–1004, https://doi.org/10.1016/j.jnucmat.2011.01.064.

[22] T. Yamamoto, Y. Wu, G.R. Odette, K. Yabuuchi, S. Kondo, A. Kimura, A dual ion irradiation study of helium-dpa interactions on cavity evolution in tempered martensitic steels and nanostructured ferritic alloys, J. Nucl. Mater. 449 (2014) 190–199, https://doi.org/10.1016/j.jnucmat.2014.01.040.

[23] B. Yao, D.J. Edwards, R.J. Kurtz, G.R. Odette, and T. Yamamoto, Microstructure Characterization of Neutron Irradiated and Helium Injected PM2000, 14YW, and Modified F82H Alloys, Fusion Materials Semiannual progress report June 2012, DOE-ER-031, 2012, p. 26.

[24] H.J. Jung, D.J. Edwards, R.J. Kurtz, T. Yamamoto, Y. Wu, G.R. Odette, Structural and chemical evolution in neutron irradiated and helium-injected ferritic ODS PM2000 alloy, J. Nucl. Mater. 484 (2017) 68–80, https://doi.org/10.1016/j.jnucmat.2016.11.022.

[25] O. Emelyanova, A. Gentils, V.A. Borodin, M.G. Ganchenkova, P.V. Vladimirov, P.S. Dzhumaev, I.A. Golovchanskiy, R. Lindau, A. Möslang, Bubble-to-void transition promoted by oxide nanoparticles in ODS-EUROFER steel ion implanted to high He content, J. Nucl. Mater. 545 (2021), 152724, https://doi.org/10.1016/j.jnucmat.2020.152724.

[26] E. Gaganidze, H.-C. Schneider, B. Dafferner, J. Aktaa, High-dose neutron irradiation embrittlement of RAFM steels, J. Nucl. Mater. 355 (2006) 83–88, https://doi.org/10.1016/j.jnucmat.2006.04.014.

[27] R. Lindau, M. Klimenkov, U. Jäntsch, A. Möslang, L. Commin, Mechanical and microstructural characterization of electron beam welded reduced activation oxide dispersion strengthened - Eurofer steel, J. Nucl. Mater. 416 (2011) 22–29, https://doi.org/10.1016/j.jnucmat.2011.01.025.

[28] M. Klimiankou, R. Lindau, A. Möslang, HRTEM Study of yttrium oxide particles in ODS steels for fusion reactor application, J. Cryst. Growth 249 (2003) 381–387, https://doi.org/10.1016/S0022-0248(02)02134-6.

[29] M. Klimiankou, R. Lindau, A. Möslang, TEM characterization of structure and composition of nanosized ODS particles in reduced activation ferritic-martensitic steels, J. Nucl. Mater. 329–333 (2004) 347–351, https://doi.org/10.1016/j.jnucmat.2004.04.083.

[30] D. Brimbal, L. Beck, O. Troeber, E. Gaganidze, P. Trocellier, J. Aktaa, R. Lindau, Microstructural characterization of Eurofer-97 and Eurofer-ODS steels before and after multi-beam ion irradiations at JANNUS Saclay facility, J. Nucl. Mater. 465 (2015) 236–244, https://doi.org/10.1016/j.jnucmat.2015.05.045.

[31] K.D. Zilnyk, V.B. Oliveira, H.R.Z. Sandim, A. Möslang, D. Raabe, Martensitic transformation in Eurofer-97 and ODS-Eurofer steels: a comparative study, J. Nucl. Mater. 462 (2015) 360–367, https://doi.org/10.1016/j.jnucmat.2014.12.112.

[32] S. Rogozhkin, A. Bogachev, O. Korchuganova, A. Nikitin, N. Orlov, A. Aleev, A. Zaluzhnyi, M. Kozodaev, T. Kulevoy, B. Chalykh, R. Lindau, J. Hoffmann, A. Möslang, P. Vladimirov, M. Klimenkov, M. Heilmaier, J. Wagner, S. Seils, Nanostructure evolution in ODS steels under ion irradiation, Nucl. Mater. Energy 9 (2016) 66–74, https://doi.org/10.1016/j.nme.2016.06.011.

[33] F. Bergner, G. Hlawacek, C. Heintze, Helium-ion microscopy, helium-ion irradiation and nanoindentation of Eurofer 97 and ODS Eurofer, J. Nucl. Mater. 505 (2018) 267–275, https://doi.org/10.1016/j.jnucmat.2017.07.054.

[34] A. Das, P. Chekhonin, E. Altstadt, F. Bergner, C. Heintze, R. Lindau, Microstructural characterization of inhomogeneity in 9Cr ODS EUROFER steel, J. Nucl. Mater. 533 (2020), 152083, https://doi.org/10.1016/j.jnucmat.2020.152083.

[35] Z. Lu, R.G. Faulkner, N. Riddle, F.D. Martino, K. Yang, Effect of heat treatment on microstructure and hardness of Eurofer 97, Eurofer ODS and T92 steels, J. Nucl. Mater. 386–388 (2009) 445–448, https://doi.org/10.1016/j.jnucmat.2008.12.152.

[36] E. Lucon, A. Leenaers, and W. Vandermeulen, Post Irradiation Examination of a Thermo-Mechanically Improved Version of EUROFER ODS, Belgium, 2006. [Online]. Available: http://inis.iaea.org/search/search.aspx?orig_q=RN:42097800.

[37] J. Fu, J.C. Brouwer, R.W.A. Hendrikx, I.M. Richardson, M.J.M. Hermans, Microstructure characterisation and mechanical properties of ODS Eurofer steel subject to designed heat treatments, Mater. Sci. Eng. A 770 (2020), 138568, https://doi.org/10.1016/j.msea.2019.138568.

[38] R. Schäublin, A. Ramar, N. Baluc, V. de Castro, M.A. Monge, T. Leguey, N. Schmid, C. Bonjour, Microstructural development under irradiation in European ODS ferritic/martensitic steels, J. Nucl. Mater. 351 (2006) 247–260, https://doi.org/10.1016/j.jnucmat.2006.02.005.

[39] M. Klimiankou, R. Lindau, A. Möslang, Direct correlation between morphology of (Fe, Cr)$_{23}$C$_6$ precipitates and impact behavior of ODS steels, J. Nucl. Mater. 367–370 (2007) 173–178, https://doi.org/10.1016/j.jnucmat.2007.03.150.

[40] C.C. Eiselt, M. Klimenkov, R. Lindau, A. Möslang, H.R.Z. Sandim, A.F. Padilha, D. Raabe, High-resolution transmission electron microscopy and electron backscatter diffraction in nanoscaled ferritic and ferritic-martensitic oxide dispersion strengthened-steels, J. Nucl. Mater. 385 (2009) 231–235, https://doi.org/10.1016/j.jnucmat.2008.11.029.

[41] M. Klimenkov, R. Lindau, A. Möslang, New insights into the structure of ODS particles in the ODS-Eurofer alloy, J. Nucl. Mater. 386–388 (2009) 553–556, https://doi.org/10.1016/j.jnucmat.2008.12.174.

[42] H.R.Z. Sandim, R.A. Renzetti, A.F. Padilha, D. Raabe, M. Klimenkov, R. Lindau, A. Möslang, Annealing behavior of ferritic-martensitic 9%Cr-ODS-Eurofer steel, Mater. Sci. Eng. A 527 (2010) 3602–3608, https://doi.org/10.1016/j.msea.2010.02.051.

[43] C. Heintze, F. Bergner, A. Ulbricht, M. Hernández-Mayoral, U. Keiderling, R. Lindau, T. Weissgärber, Microstructure of oxide dispersion strengthened Eurofer and iron-chromium alloys investigated by means of small-angle neutron scattering and transmission electron microscopy, J. Nucl. Mater. 416 (2011) 35–39, https://doi.org/10.1016/j.jnucmat.2010.11.102.

[44] H.R.Z. Sandim, R.A. Renzetti, A.F. Padilha, A. Möslang, R. Lindau, D. Raabe, Annealing behavior of RAFM ODS-Eurofersteel, Fusion Sci. Techn. 61 (2012) 136–140, https://doi.org/10.13182/FST12-A13379.

[45] P. Fernández, A.M. Lancha, J. Lapeña, M. Hernández-Mayoral, Metallurgical characterization of the reduced activation ferritic/martensitic steel Eurofer'97 on as-received condition, Fusion Eng. Des. 58–59 (2001) 787–792, https://doi.org/10.1016/S0920-3796(01)00563-4.

[46] P. Fernández, A.M. Lancha, J. Lapeña, M. Serrano, M. Hernández-Mayoral, Metallurgical properties of reduced activation of martensitic steel Eurofer'97 in the as-received condition and after thermal ageing, J. Nucl. Mater. 307–311 (2002) 495–499, https://doi.org/10.1016/S0022-3115(02)01013-9.

[47] M. Klimenkov, R. Lindau, E. Materna-Morris, A. Möslang, TEM characterization of precipitates in EUROFER 97, Progr. Nucl. Energy 57 (2012) 8–13, https://doi.org/10.1016/j.pnucene.2011.10.006.

[48] A. Gentils, C. Cabet, Investigating radiation damage in nuclear energy materials using JANNuS multiple ion beams, Nucl. Instrum. Methods Phys. Res. B 447 (2019) 107–112, https://doi.org/10.1016/j.nimb.2019.03.039.

[49] J.F. Ziegler, J.P. Biersack, U. Littmark, The stopping and range of ions in matter, Pergamon, NY, 1985.

[50] Electron Backscatter Diffraction in Materials Science. A.J. Schwartz, M. Kumar, B. L. Adams, and D. P. Field, Eds., Boston, MA: Springer US, 2009. doi: 10.1007/978-0-387-88136-2.

[51] T. Malis, S.C. Cheng, R.F. Egerton, EELS log-ratio technique for specimen-thickness measurement in the TEM, J. Electron Microsc. Tech. 8 (1988) 193–200, https://doi.org/10.1002/jemt.1060080206.

[52] K. Iakoubovskii, K. Mitsuishi, Y. Nakayama, K. Furuya, Thickness measurements with electron energy loss spectroscopy, Microsc. Res. Tech. 71 (2008) 626–631, https://doi.org/10.1002/jemt.20597.

[53] M. Kirk, X. Yi, M. Jenkins, Characterization of irradiation defect structures and densities by transmission electron microscopy, J. Mater. Res. 30 (2015) 1195–1201, https://doi.org/10.1557/jmr.2015.19.

[54] B. Yao, D.J. Edwards, R.J. Kurtz, G.R. Odette, T. Yamamoto, Multislice simulation of transmission electron microscopy imaging of helium bubbles in Fe, J. Electron Microsc. (Tokyo) 61 (2012) 393–400, https://doi.org/10.1093/jmicro/dfs065.

[55] M. Yamamoto, S. Ukai, S. Hayashi, T. Kaito, S. Ohtsuka, Formation of residual ferrite in 9Cr-ODS ferritic steels, Mater. Sci. Eng. A 527 (2010) 4418–4423, https://doi.org/10.1016/j.msea.2010.03.079.

[56] L.L. Hsiung, M.J. Fluss, S.J. Tumey, B.W. Choi, Y. Serruys, F. Willaime, A. Kimura, Formation mechanism and the role of nanoparticles in Fe-Cr ODS steels developed for radiation tolerance, Phys. Rev. B 82 (2010) 1–13, https://doi.org/10.1103/PhysRevB.82.184103.

[57] M. Roldán, P. Fernández, J. Rams, D. Jiménez-Rey, E. Materna-Morris, M. Klimenkov, Comparative study of helium effects on EU-ODS EUROFER and EUROFER97 by nanoindentation and TEM, J. Nucl. Mater. 460 (2015) 226–234, https://doi.org/10.1016/j.jnucmat.2015.02.025.

[58] A. Bhattacharya, E. Meslin, J. Henry, B. Décamps, A. Barbu, Dramatic reduction of void swelling by helium in ion-irradiated high purity α-iron, Mater. Res. Lett. 6 (2018) 372–377, https://doi.org/10.1080/21663831.2018.1462266.

[59] D. Brimbal, E. Meslin, J. Henry, B. Décamps, A. Barbu, He and Cr effects on radiation damage formation in ion-irradiated pure iron and Fe-5.40wt.% Cr: a transmission electron microscopy study, Acta Mater. 61 (2013) 4757–4764, https://doi.org/10.1016/j.actamat.2013.04.070.

[60] D. Sun, R. Li, J. Ding, S. Huang, P. Zhang, Z. Lu, J. Zhao, Helium behavior in oxide dispersion strengthened (ODS) steel: insights from ab initio modeling, J. Nucl. Mater. 499 (2018) 71–78, https://doi.org/10.1016/j.jnucmat.2017.10.073.